A new mixed Boltzmann-BGK model for mixtures solved with an IMEX finite volume scheme on unstructured meshes

A new mixed Boltzmann-BGK model for mixtures solved with an IMEX finite volume scheme on unstructured meshes

Marzia Bisi[a], Walter Boscheri[*b,c], Giacomo Dimarco[b,c], Maria Groppi[a], Giorgio Martalò[a]

[a]*Department of Mathematical, Physical and Computer Sciences, University of Parma, Parco Area delle Scienze 53/A, 43124 Parma, Italy*
[b]*Department of Mathematics and Computer Science, University of Ferrara, Via Machiavelli 30, 44121 Ferrara, Italy*
[c]*Center for Modeling, Computing and Statistics CMCS, University of Ferrara, Via Muratori 9, 44121 Ferrara, Italy*

Abstract

In this work, we consider a novel model for a binary mixture of inert gases. The model, which preserves the structure of the original Boltzmann equations, combines integro-differential collision operators with BGK relaxation terms in each kinetic equation: the first involving only collisions among particles of the same species, while the second ones taking into account the inter–species interactions. We prove consistency of the model: conservation properties, positivity of all temperatures, H-theorem and convergence to a global equilibrium in the shape of a global Maxwell distribution. We also derive hydrodynamic equations under different collisional regimes. In a second part, to numerically solve the governing equations, we introduce a class of time and space high order finite volume schemes that are able to capture the behaviors of the different hydrodynamic limit models: the classical Euler equations as well as the multi-velocities and temperatures Euler system. The methods work by integrating the distribution functions over arbitrarily shaped and closed control volumes in 2D using Central Weighted ENO (CWENO) techniques and make use of spectral methods for the approximation of the Boltzmann integrals with high order Implicit-Explicit (IMEX) Runge Kutta schemes. For these methods, we prove accuracy and preservation of the discrete asymptotic states. In the numerical section we first show that the methods indeed possess the theoretical order of accuracy for different regimes and second we analyse their capacity in solving different two dimensional problems arising in kinetic theory. To speed up the computational time, all simulations are run with MPI parallelization on 64 cores, thus showing the potentiality of the proposed methods to be used for HPC (High Performance Computing) on massively parallel architectures.

Keywords: Inert gas mixtures, Kinetic Boltzmann equations, Hydrodynamic limit, Implicit-Explicit Runge Kutta, Unstructured meshes, High order of accuracy in space and time.

1. Introduction

Kinetic theory for inert or reactive gas mixtures has been widely investigated in recent years, see for instance [33, 54, 42, 15] and the references therein. Boltzmann equations for inert mixtures, as well as their major mathematical properties, may be found also in classical books [22, 23, 35] but, since their numerical simulation in realistic physical problems is not an easy task to accomplish, many simpler kinetic approximations have been proposed in the past. In this respect, the most usual approach consists in suitable generalizations of the BGK relaxation model proposed by Bhatnagar, Gross and Krook in [8] for a single gas. The idea of such kind of models comes from the fact that the dynamics of the system drives the configuration to relax towards a Maxwellian state, so that collisions cause a change rate for the distribution which is proportional to the difference between the distribution itself and a Maxwellian attractor. The extension of the BGK model to a gas mixture is not unique, since in the Maxwellian attractors several free parameters appear. These may be suitably chosen in order to reproduce some basic properties of

*Corresponding author
Email addresses: marzia.bisi@unipr.it (Marzia Bisi), walter.boscheri@unife.it (Walter Boscheri*), giacomo.dimarco@unife.it (Giacomo Dimarco), maria.groppi@unipr.it (Maria Groppi), giorgio.martalo@unipr.it (Giorgio Martalò)

the original Boltzmann operators. A milestone in the rigorous mathematical approach for the construction of BGK operators is the work of Andries, Aoki and Perthame [2], where the kinetic equation for each species is governed by a unique relaxation operator, with auxiliary parameters in the Maxwellian attractor taking into account the effects due to collisions with whatever other species. This way of modeling collisions among different species has given rise to various applications and generalizations, also to reactive mixtures [9] or to mixtures of monatomic and polyatomic gases [13, 14]. In spite of its simplicity, this model is able to preserve correct collision invariants and collision equilibria, fulfillment of Boltzmann H–theorem, positivity of distribution functions and temperatures. However, a drawback of having a unique BGK operator for each constituent is that only global conservation laws can be imposed, hence loosing the details of bi–species exchanges. For this reason another kind of models has been widely considered in the literature [50, 43, 47], with a sum of BGK operators for each species, each one describing the interactions with any other species (equal or different). Also the recent developments introduced in [15] fit into this research line, and the proposed BGK model, that will be used also in this paper, aims at preserving the structure of the original Boltzmann equations, imposing that each bi–species BGK operator preserves the bi–species Boltzmann exchange rates of momentum and energy, for general intermolecular potentials. The behaviors of the different BGK models for mixtures studied in [2, 9, 15] have been recently numerically compared in [17] also in their hydrodynamic limits.

From the numerical point of view, modern deterministic solvers are often based on a spectral method for the solution of the Boltzmann collision operator [52, 37]. Typically a discrete velocity model (DVM) [16] is used for the discretization of the velocity space, while different spatial discretization techniques can be employed in the physical space, e.g. finite element [34], finite volume [19, 24, 6] or discontinuous Galerkin [20, 45, 56] schemes. Particular care must be devoted to the time discretization, which has to satisfy the so-called asymptotic preserving (AP) property, thus ensuring that the numerical scheme is capable of retrieving a consistent discretization of the limit model in the stiff relaxation limit of the governing equations. A well-suited class of methods that satisfies this requirement is represented by Implicit-Explicit (IMEX) Runge-Kutta (RK) methods [29, 46, 36, 27, 53, 25, 30, 49], where the collisional fast scale is discretized implicitly while keeping the transport part explicit, hence allowing for time steps which are independent of the stiffness of the problem. Linear Multistep Methods [4, 31, 20] have also been investigated in the literature, which are proven to be more efficient and more accurate compared to Runge-Kutta time stepping techniques in many situations. For monatomic gas mixtures, in [48] a fast Fourier method is adopted,a moment method is devised in [1] to approximate the Maxwell-Stefan limit of a multispecies gas, while in [5] a kinetic multispecies model is solved at the aid of a projective integration technique in time, where the collisions among the species are modeled with simpler BGK-type operators. Gas-kinetic schemes for binary gas mixtures have been presented in [58, 57] and those methods are able to properly capture the two-species Navier-Stokes equations with the correct Prandtl number, hence considering heat conduction effects as well.

In this paper, in order to preserve as much as possible the accuracy of the Boltzmann description but with a kinetic system manageable from the computational point of view, we propose and investigate a mixed Boltzmann–BGK model for a binary mixture, in which collisions occurring within the same species (intra–species) are modelled by Boltzmann operators, while interactions between the two constituents (inter–species) are described by the BGK operators given in [15], that represent the relaxation model for mixtures with the closest structure to the Boltzmann one. To the best of our knowledge, this hybrid model has never been investigated before. For this reason, we first show in the rest of the paper that it fulfills the basic mathematical properties of the Boltzmann equations that we want to approximate. Specifically, we prove that the unique collision equilibrium admitted by this kinetic model is the expected (Boltzmann) one: namely distributions accommodated at a Maxwellian shape, sharing a common mean velocity and a common temperature. The crucial step to get this result will be the entropy dissipation estimate, namely the Boltzmann H–theorem, that we demonstrate to be valid even for the present Boltzmann–BGK model. As already discussed for Boltzmann or BGK models [42, 12, 10], having a sum of binary collision operators in the kinetic equations allows to investigate also hydrodynamic regimes in which some collisions are more frequent than the others. We present the Euler equations corresponding to our mixed model, both in a situation with all collisions dominant and also in the case in which only collisions within the same species play the dominant role. This latter regime turns out to be useful to describe some phenomena in plasma physics, where the mass for electrons is much smaller than for ions [54], and also in general ε–mixtures of gases having very different masses, where energy exchanges between particles with disparate masses occur more slowly than between particles of the same species [39].

In a second part, the proposed kinetic model will be solved with a fully second order accurate asymptotic preserving numerical method in space and time, along the lines of some recent contributions in the context of finite

volume [21, 19] and discontinuous Galerkin schemes [20]. The computational domain is discretized with general unstructured control volumes made of polygons, where a CWENO reconstruction operator is used to increase the spatial accuracy of a finite volume method. The velocity space is approximated relying on a discrete velocity model on a two-dimensional Cartesian mesh, while the Boltzmann collision operator is evaluated by means of a fast spectral method based on Fourier modes. Finally, time integration is carried out employing an IMEX Runga-Kutta method. For this particular class of methods, we show that they are able to retrieve a consistent discretization of the hydrodynamic limit models derived from the theory, in which the different collisional scales grow to infinity. The resulting scheme is therefore numerically shown to be independent of the stiffness of the problem, thus allowing large time steps to be adopted which eventually improve the computational efficiency of the algorithm. The scheme is implemented under MPI parallelization and tested on several cores.

The rest of the work is organized in the following manner. In Section 2 we present the mixed Boltzmann–BGK equations and also their dimensionless version. We prove the consistency of the model, namely fulfillment of the expected entropy dissipation (Boltzmann H–theorem) and existence and uniqueness of a steady (Maxwellian) configuration. We also derive Euler hydrodynamic equations in two different asymptotic limits, namely a regime with all collisions dominant and a case with intra–species collisions more frequent than the others. In Section 3, the numerical method is presented, which is composed of three main discretizations: (i) the discrete velocity model, (ii) the spatial discretization with the CWENO reconstruction operator, (iii) the time integration technique with asymptotic preserving IMEX Runge-Kutta methods. The proof of the asymptotic preservation and accuracy is also reported in this part. The spectral method is briefly discussed after the introduction of the discrete velocy model while the details on the spectral method for the approximation of the Boltzmann collision operator can be found in [52, 37] for the theoretical part and in [19] for applications. Section 4 is devoted to the numerical validation of the novel model, therefore convergence studies as well as other benchmark test cases are presented on unstructured polygonal meshes for different collision regimes. Conclusions and future investigations are then drawn in Section 5.

2. Kinetic equations for a binary mixture

We consider a binary mixture of monatomic gases with masses m_i, $i = 1, 2$, and distributions $f_i(t, \mathbf{x}, \mathbf{v})$, $i = 1, 2$, depending on time $t \in \mathbb{R}_+$, position $\mathbf{x} \in \mathbb{R}^{d_x}$ in dimension d_x, and molecular velocity $\mathbf{v} \in \mathbb{R}^{d_v}$. Number densities n_i, mean velocities $\mathbf{u}_i$ and temperatures T_i of both constituents are recovered as moments of the distributions themselves as

$$n_i = \int_{\mathbb{R}^d} f_i(\mathbf{v})\, d\mathbf{v}\,, \qquad \mathbf{u}_i = \frac{1}{n_i}\int_{\mathbb{R}^d} \mathbf{v}\, f_i(\mathbf{v})\, d\mathbf{v}\,, \qquad T_i = \frac{m_i}{d\, n_i}\int_{\mathbb{R}^d} |\mathbf{v}-\mathbf{u}|^2 f_i(\mathbf{v})\, d\mathbf{v}\,, \tag{1}$$

where we have assumed that $d_x = d_v = d$ from now on even if not strictly necessary. The evolution of the system is assumed to be governed by a new mixed Boltzmann–BGK model. Specifically, intra–species collisions are modeled by Boltzmann operators while inter–species collisions are described by relaxation–type operators. The associated kinetic equations read then as

$$\begin{aligned} \frac{\partial f_1}{\partial t} + \mathbf{v}\cdot\nabla_{\mathbf{x}} f_1 &= Q_{11}(f_1, f_1) + \hat{Q}_{12}(f_1, f_2) \\ \frac{\partial f_2}{\partial t} + \mathbf{v}\cdot\nabla_{\mathbf{x}} f_2 &= \hat{Q}_{21}(f_2, f_1) + Q_{22}(f_2, f_2). \end{aligned} \tag{2}$$

Boltzmann terms modeling collisions within each component [22] are provided by the operators

$$Q_{ii}(f_i, f_i) = \int_{\mathbb{R}^d}\int_{S^{d-1}} g_{ii}(|\mathbf{y}|, \hat{\mathbf{y}}\cdot\boldsymbol{\omega})\Big[f_i(\mathbf{v}'_{ii})\, f_i(\mathbf{w}'_{ii}) - f_i(\mathbf{v})\, f_i(\mathbf{w})\Big]\, d\mathbf{w}\, d\boldsymbol{\omega}\,, \qquad i = 1, 2, \tag{3}$$

with $\mathbf{y} = \mathbf{v} - \mathbf{w}$ the relative velocity and $\hat{\mathbf{y}} = \frac{\mathbf{y}}{|\mathbf{y}|}$ its direction. Moreover, g_{ii} is the so-called collisional cross section depending only on the type of interactions between particles, S^{d-1} is the $d-1$ unit sphere with d the dimension of the velocity space, ω is the vector spanning the unit sphere S^{d-1} and finally w is the pre-collisional velocity of the particle colliding with the one at velocity v, leading to post collisional velocity pair (v'_{ii}, w'_{ii}). In particular, the velocities $(\mathbf{v}'_{ii}, \mathbf{w}'_{ii})$ in (3) are related to $(\mathbf{v}, \mathbf{w})$ by

$$\mathbf{v}'_{ii} = \frac{1}{2}(\mathbf{v}+\mathbf{w}) + \frac{1}{2}|\mathbf{y}|\,\boldsymbol{\omega}\,, \qquad \mathbf{w}'_{ii} = \frac{1}{2}(\mathbf{v}+\mathbf{w}) - \frac{1}{2}|\mathbf{y}|\,\boldsymbol{\omega}\,. \tag{4}$$

The interactions between different constituents are instead described by BGK–type relaxation operators. Among the many consistent BGK approximations for inert gas mixtures available in the literature [2, 43, 47], here we adopt the model proposed in [15], in which each bi–species relaxation term reproduces the exchange rate of momentum and energy of the corresponding Boltzmann operator. More precisely, we set

$$\hat{Q}_{ik} = \nu_{ik}\,(M_{ik} - f_i)\,, \qquad (i,k) = (1,2)\,,\,(2,1)\,, \tag{5}$$

where ν_{ik} are suitable collision frequencies, while the attractors

$$M_{ik} = n_i M\left(\mathbf{v}, \mathbf{u}_{ik}, \frac{T_{ik}}{m_i}\right) = n_i \left(\frac{m_i}{2\pi T_{ik}}\right)^{d/2} \exp\left(-\frac{m_i}{2T_{ik}}\,|\mathbf{v} - \mathbf{u}_{ik}|^2\right) \tag{6}$$

are Maxwellian distributions depending on auxiliary parameters $\mathbf{u}_{ik}$ and T_{ik} which are determined by imposing that

$$\int_{\mathbb{R}^d} \mathbf{v}\,\hat{Q}_{ik}\,d\mathbf{v} = \int_{\mathbb{R}^d} \mathbf{v}\,Q_{ik}(f_i,f_k)\,d\mathbf{v}\,, \qquad \int_{\mathbb{R}^d} |\mathbf{v}|^2\,\hat{Q}_{ik}\,d\mathbf{v} = \int_{\mathbb{R}^d} |\mathbf{v}|^2\,Q_{ik}(f_i,f_k)\,d\mathbf{v}\,, \tag{7}$$

with $Q_{ik}(f_i,f_k)$ denoting the bi–species Boltzmann operator [22]

$$Q_{ik}(f_i,f_k) = \int_{\mathbb{R}^d}\int_{S^{d-1}} g_{ik}(|\mathbf{y}|,\hat{\mathbf{y}}\cdot\boldsymbol{\omega})\Big[f_i(\mathbf{v}'_{ik})\,f_k(\mathbf{w}'_{ik}) - f_i(\mathbf{v})\,f_k(\mathbf{w})\Big]\,d\mathbf{w}\,d\boldsymbol{\omega}\,, \qquad (i,k) = (1,2)\,,\,(2,1)\,.$$

Left hand sides of equalities (7), relevant to BGK contributions, may be straightforwardly computed, leading to

$$\nu_{ik}\,n_i\,(\mathbf{u}_{ik} - \mathbf{u}_i) = \int_{\mathbb{R}^d} \mathbf{v}\,Q_{ik}(f_i,f_k)\,d\mathbf{v}\,,$$

$$\nu_{ik}\,n_i\left(d\,\frac{T_{ik} - T_i}{m_i} + |\mathbf{u}_{ik}|^2 - |\mathbf{u}_i|^2\right) = \int_{\mathbb{R}^d} |\mathbf{v}|^2\,Q_{ik}(f_i,f_k)\,d\mathbf{v}\,.$$

The computation of Boltzmann contributions may be done explicitly only for Maxwell molecules, having the cross section g_{ik} independent of $|\mathbf{y}|$; in this case, skipping intermediate computations we get

$$\mathbf{u}_{ik} = (1 - a_{ik})\,\mathbf{u}_i + a_{ik}\,\mathbf{u}_k\,, \qquad T_{ik} = (1 - b_{ik})\,T_i + b_{ik}\,T_k + \gamma_{ik}\,|\mathbf{u}_i - \mathbf{u}_k|^2\,,$$

$$a_{ik} = \frac{\mu\,n_k m_k}{\nu_{ik}(m_i + m_k)}\,, \qquad b_{ik} = \frac{2\,a_{ik}\,m_i}{m_i + m_k}\,, \qquad \gamma_{ik} = \frac{m_i\,a_{ik}}{d}\left(\frac{2\,m_k}{m_i + m_k} - a_{ik}\right), \tag{8}$$

where the parameter μ is related to the Boltzmann cross section as

$$\mu\,\hat{\mathbf{y}} = \int_{S^{d-1}} (\hat{\mathbf{y}} - \boldsymbol{\omega})\,g_{12}(\hat{\mathbf{y}}\cdot\boldsymbol{\omega})\,d\boldsymbol{\omega} = \int_{S^{d-1}} (\hat{\mathbf{y}} - \boldsymbol{\omega})\,g_{21}(\hat{\mathbf{y}}\cdot\boldsymbol{\omega})\,d\boldsymbol{\omega}\,. \tag{9}$$

For general intermolecular potentials, the computation of contributions on the right hand sides of (7) involves the angular integral

$$\widetilde{g}(|\mathbf{y}|)\,\hat{\mathbf{y}} = \int_{S^{d-1}} (\hat{\mathbf{y}} - \boldsymbol{\omega})\,g_{12}(|\mathbf{y}|,\hat{\mathbf{y}}\cdot\boldsymbol{\omega})\,d\boldsymbol{\omega} = \int_{S^{d-1}} (\hat{\mathbf{y}} - \boldsymbol{\omega})\,g_{21}(|\mathbf{y}|,\hat{\mathbf{y}}\cdot\boldsymbol{\omega})\,d\boldsymbol{\omega},$$

with $\widetilde{g}$ depending on the relative speed. In order to complete the construction of the BGK operator, we approximate $\widetilde{g}(|\mathbf{v} - \mathbf{w}|)$ by its value in some typical point, i.e. $\widetilde{g}(|\mathbf{v} - \mathbf{w}|) \cong \widetilde{g}(\bar{z})$, where we choose as reference value $\bar{z}$ a suitable average of the relative velocity defined as

$$\bar{z} = \left(\frac{1}{n_1\,n_2}\int_{\mathbb{R}^d}\int_{\mathbb{R}^d} |\mathbf{v} - \mathbf{w}|^2\,f_1(\mathbf{v})\,f_2(\mathbf{w})\,d\mathbf{v}\,d\mathbf{w}\right)^{1/2} = \left[d\left(\frac{T_1}{m_1} + \frac{T_2}{m_2}\right) + |\mathbf{u}_1 - \mathbf{u}_2|^2\right]^{1/2}.$$

This approach leads exactly to the formulas (8) obtained in the Maxwell molecules case, but with the parameter $\mu = \widetilde{g}(\bar{z})$.

Collision frequencies ν_{ik}, with $(i,k) = (1,2)$ or $(2,1)$, are free parameters; as already noticed in the past, their choice does not represent a trivial issue and various possible strategies have been proposed [11, 41] for different BGK models. For the BGK operators used in the present paper, in [15] it has been proved that auxiliary temperatures T_{ik} defined in (8) are strictly positive only if $\nu_{ik} \geq \mu\,n_k/2$. In order to fulfill this positivity constraint we adopt from here on the choice $\nu_{ik} = \mu\,n_k$, and in numerical simulations we consider Maxwell molecules interactions.

2.1. Dimensionless setting and properties of the kinetic model

In this section we derive the dimensionless form of our kinetic model (2). To this aim, we introduce the following normalizations

$$\begin{aligned} &\widetilde{f_1} = \left(\frac{T_0}{m_1}\right)^{d/2} \frac{f_1}{n_0}\,, \qquad \widetilde{f_2} = \left(\frac{T_0}{m_1}\right)^{d/2} \frac{f_2}{n_0}\,, \qquad \widetilde{n}_1 = \frac{n_1}{n_0}\,, \qquad \widetilde{n}_2 = \frac{n_2}{n_0}\,, \\ &\widetilde{T}_1 = \frac{T_1}{T_0}\,, \qquad \widetilde{T}_2 = \frac{T_2}{T_0}\,, \qquad \widetilde{\mathbf{v}} = \frac{\mathbf{v}}{\sqrt{\frac{T_0}{m_1}}}\,, \qquad \widetilde{\mathbf{u}}_1 = \frac{\mathbf{u}_1}{\sqrt{\frac{T_0}{m_1}}}\,, \qquad \widetilde{\mathbf{u}}_2 = \frac{\mathbf{u}_2}{\sqrt{\frac{T_0}{m_1}}}\,, \end{aligned} \tag{10}$$

where n_0 and T_0 are suitable reference number density and temperature, respectively. Moreover, we introduce the mass ratio $m = m_2/m_1$. We scale also time and space variables as

$$\widetilde{t} = \nu\, t\,, \qquad \widetilde{\mathbf{x}} = \frac{\nu\, \mathbf{x}}{\sqrt{\frac{T_0}{m_1}}}\,, \tag{11}$$

where ν is a suitable average collision frequency. Since in the following sections we aim at considering problems in which collisions play the dominant role, but intra–species and inter–species rates of collisions could have different orders of magnitude, we rescale collision frequencies as

$$\widetilde{\nu}_{12} = \frac{\varepsilon\, \nu_{12}}{\alpha\, \nu}\,, \qquad \widetilde{\nu}_{21} = \frac{\varepsilon\, \nu_{21}}{\alpha\, \nu}\,, \qquad \widetilde{g}_{11} = \frac{\varepsilon\, n_0}{\nu}\, g_{11}\,, \qquad \widetilde{g}_{22} = \frac{\varepsilon\, n_0}{\nu}\, g_{22}\,,$$

with ε and α suitable constants. Finally, we note that we can take $\widetilde{\mu} = \varepsilon\, \mu\, n_0/(\alpha\, \nu)$, since the unit measure of coefficient μ differs from the one of the collision frequencies only by a number density factor.

Substituting all these quantities into equations (2), and omitting all tildes ($\sim$), the novel model equations in dimensionless form may be cast as

$$\begin{aligned} &\frac{\partial f_1}{\partial t} + \mathbf{v}\cdot\nabla_{\mathbf{x}} f_1 = \frac{1}{\varepsilon}\, Q_{11}(f_1, f_1) + \frac{\alpha}{\varepsilon}\, \nu_{12}\, (M_{12} - f_1) \\ &\frac{\partial f_2}{\partial t} + \mathbf{v}\cdot\nabla_{\mathbf{x}} f_2 = \frac{\alpha}{\varepsilon}\, \nu_{21}\, (M_{21} - f_2) + \frac{1}{\varepsilon}\, Q_{22}(f_2, f_2) \end{aligned} \tag{12}$$

where the nondimensional Maxwellian attractors are now given by

$$M_{12} = n_1 \left(\frac{1}{2\pi T_{12}}\right)^{d/2} \exp\left(-\frac{|\mathbf{v} - \mathbf{u}_{12}|^2}{2T_{12}}\right), \qquad M_{21} = n_2 \left(\frac{m}{2\pi\, T_{21}}\right)^{d/2} \exp\left(-\frac{m\,|\mathbf{v} - \mathbf{u}_{21}|^2}{2T_{21}}\right). \tag{13}$$

The auxiliary parameters $\mathbf{u}_{12}$, $\mathbf{u}_{21}$, T_{12}, T_{21} take the form

$$\begin{aligned} &\mathbf{u}_{12} = (1 - a_{12})\, \mathbf{u}_1 + a_{12}\, \mathbf{u}_2\,, \qquad T_{12} = (1 - b_{12})\, T_1 + b_{12}\, T_2 + \gamma_{12}\, |\mathbf{u}_1 - \mathbf{u}_2|^2\,, \\ &a_{12} = \mu\, \frac{n_2}{\nu_{12}} \frac{m}{1+m}\,, \qquad b_{12} = 2\, a_{12}\, \frac{1}{1+m}\,, \qquad \gamma_{12} = \frac{a_{12}}{d} \left(\frac{2\, m}{1+m} - a_{12}\right), \end{aligned} \tag{14}$$

and

$$\begin{aligned} &\mathbf{u}_{21} = (1 - a_{21})\, \mathbf{u}_2 + a_{21}\, \mathbf{u}_1\,, \qquad T_{21} = (1 - b_{21})\, T_2 + b_{21}\, T_1 + \gamma_{21}\, |\mathbf{u}_1 - \mathbf{u}_2|^2\,, \\ &a_{21} = \mu\, \frac{n_1}{\nu_{21}}\, \frac{1}{1+m}\,, \qquad b_{21} = 2\, a_{21}\, \frac{m}{1+m}\,, \qquad \gamma_{21} = \frac{m\, a_{21}}{d} \left(\frac{2}{1+m} - a_{21}\right). \end{aligned} \tag{15}$$

In the specific case of Maxwell molecules, the above terms simplify since by assumption we have $\nu_{12} = n_2\, \mu$ and $\nu_{21} = n_1\, \mu$ with constant μ and the coefficients become

$$\begin{aligned} &a_{12} = \frac{m}{1+m}\,, \qquad a_{21} = \frac{1}{1+m}\,, \qquad b_{12} = b_{21} = \frac{2\, m}{(1+m)^2}\,, \\ &\gamma_{12} = \frac{1}{d} \left(\frac{m}{1+m}\right)^2, \qquad \gamma_{21} = \frac{\gamma_{12}}{m}\,. \end{aligned}$$

Since BGK operators in our model have been derived by imposing constraints (7), that are nothing but preservation of Boltzmann bi–species momentum and energy exchanges, the mixed Boltzmann–BGK model (12) ensures conservation of species number densities, global mixture velocity and global temperature, as it occurs for classical Boltzmann equations.

Concerning steady configurations, we can observe that the expected physical steady state, namely the pair of Maxwellians (M_1, M_2) with

$$M_1 = n_1 \left(\frac{1}{2\pi T}\right)^{d/2} \exp\left(-\frac{|\mathbf{v}-\mathbf{u}|^2}{2T}\right) \quad \text{and} \quad M_2 = n_2 \left(\frac{m}{2\pi T}\right)^{d/2} \exp\left(-\frac{m|\mathbf{v}-\mathbf{u}|^2}{2T}\right), \tag{16}$$

and

$$\mathbf{u}_1 = \mathbf{u}_2 = \mathbf{u} \quad \text{and} \quad T_1 = T_2 = T\,, \tag{17}$$

turns out to be an equilibrium of (12). In fact, from (8) under the above hypothesis we get

$$\mathbf{u}_{12} = \mathbf{u}_{21} = \mathbf{u} \quad \text{and} \quad T_{12} = T_{21} = T\,, \tag{18}$$

and hence

$$M_{12} = M_1 \quad \text{and} \quad M_{21} = M_2\,. \tag{19}$$

This implies that $(M_{12} - f_1) = (M_{21} - f_2) = 0$. Then, since also $Q_{11} = Q_{22} = 0$ under the same hypothesis $f_1 = M_1$ and $f_2 = M_2$, we have that the pair (M_1, M_2) represents a possible equilibrium of the system.

2.2. Uniqueness and stability of the steady state configuration for the mixed Boltzmann–BGK model

In this part, we prove that the equilibrium steady state (16) is indeed the unique admissible steady configuration for (12) and that, moreover, it is asymptotically stable. To this aim, we show that the classical Boltzmann H–functional

$$H = \int_{\mathbb{R}^d} f_1(\mathbf{v}) \log f_1(\mathbf{v}) d\mathbf{v} + \int_{\mathbb{R}^d} f_2(\mathbf{v}) \log f_2(\mathbf{v}) d\mathbf{v} \tag{20}$$

is a Lyapunov functional (describing the entropy dissipation) for the mixed model (12). In order to avoid unessential multiplicative constants we write the proof in the case $\varepsilon = \alpha = 1$. The time derivative of the functional (20) (in space homogeneous conditions) reads as

$$\begin{aligned} \dot{H} &= \int_{\mathbb{R}^d} Q_{11}(f_1, f_1) \log f_1 \, d\mathbf{v} + \nu_{12} \int_{\mathbb{R}^d} (M_{12} - f_1) \log f_1 \, d\mathbf{v} \\ &+ \nu_{21} \int_{\mathbb{R}^d} (M_{21} - f_2) \log f_2 \, d\mathbf{v} + \int_{\mathbb{R}^d} Q_{22}(f_2, f_2) \log f_2 \, d\mathbf{v}\,. \end{aligned} \tag{21}$$

The first and last terms appear also in the classical one–species H–theorem [22] and may be cast as

$$\begin{aligned} &\int_{\mathbb{R}^d} Q_{ii}(f_i, f_i) \log f_i \, d\mathbf{v} = \\ &-\frac{1}{4} \int_{\mathbb{R}^d \times \mathbb{R}^d \times \mathbb{S}^{d-1}} g_{ii} \log\left(\frac{f_i(\mathbf{v}'_{ii}) f_i(\mathbf{w}'_{ii})}{f_i(\mathbf{v}) f_i(\mathbf{w})}\right)\left(\frac{f_i(\mathbf{v}'_{ii}) f_i(\mathbf{w}'_{ii})}{f_i(\mathbf{v}) f_i(\mathbf{w})} - 1\right) f_i(\mathbf{v}) f_i(\mathbf{w}) d\mathbf{v} d\mathbf{w} d\boldsymbol{\omega} \le 0\,. \end{aligned} \tag{22}$$

Concerning the remaining terms in (21), using the inequality

$$(y - x) \log x \le y(\log y - 1) - x(\log x - 1),$$

we can estimate

$$\int_{\mathbb{R}^d} (M_{ik} - f_i) \log f_i d\mathbf{v} \le \int_{\mathbb{R}^d} (M_{ik} \log M_{ik} - f_i \log f_i) \, d\mathbf{v} - \int_{\mathbb{R}^d} (M_{ik} - f_i) \, d\mathbf{v}\,. \tag{23}$$

The last integral vanishes since M_{ik} and f_i have the same number density. In the remaining integral, one can make use of the classical result in [22], that is

$$\int_{\mathbb{R}^d} f_i \log f_i d\mathbf{v} \geq \int_{\mathbb{R}^d} \bar{M}_i \log \bar{M}_i d\mathbf{v}\,,$$

where $\bar{M}_i$ denotes the Maxwellian distribution having macroscopic fields n_i, $\mathbf{u}_i$ and T_i of the i–th constituent, leading to

$$\int_{\mathbb{R}^d} (M_{ik} - f_i) \log f_i d\mathbf{v} \leq \int_{\mathbb{R}^d} \left(M_{ik} \log M_{ik} - \bar{M}_i \log \bar{M}_i \right) d\mathbf{v} = -\frac{d}{2} n_i \log\left(\frac{T_{ik}}{T_i}\right), \tag{24}$$

where the last equality can be obtained by direct computations. Recalling now the definitions of T_{12} and T_{21} in (14) and (15), respectively, and the inequality

$$\log[(1-b)x + by] \geq (1-b)\log x + b\,\log y,$$

for $(i,k) = (1,2)$ or $(2,1)$ we obtain

$$\log(T_{ik}) - \log(T_i) \geq b_{ik}\,\log\left(\frac{T_k}{T_i}\right). \tag{25}$$

In conclusion, by using the relation

$$n_1 \nu_{12} b_{12} = n_2 \nu_{21} b_{21}\,, \tag{26}$$

we eventually get the following inequality

$$\begin{aligned} &\nu_{12} \int_{\mathbb{R}^d} (M_{12} - f_1) \log f_1 d\mathbf{v} + \nu_{21} \int_{\mathbb{R}^d} (M_{21} - f_2) \log f_2 d\mathbf{v} \leq \\ &-\frac{d}{2} n_1 \nu_{12} b_{12} \log\left(\frac{T_2}{T_1}\right) - \frac{d}{2} n_2 \nu_{21} b_{21} \log\left(\frac{T_1}{T_2}\right) = 0\,, \end{aligned} \tag{27}$$

and this concludes the proof of the entropy dissipation.

Moreover, the uniqueness of the equilibrium (16) follows from the condition $\dot{H} = 0$. Indeed, if (F_1, F_2) is an equilibrium, then it must hold $\dot{H}(F_1, F_2) = 0$. Since $\dot{H}$ is provided by the sum of three non positive contributions, i.e. the first and the last terms in (21) (estimated in (22)) and the sum of the BGK ones (estimated in (27)), all of them must vanish. From the Boltzmann terms (the first and last in (21)), it follows by standard arguments that F_i is a Maxwellian function depending on its own mean velocity $\mathbf{u}_i$ and temperature T_i, i.e $F_i = \bar{M}_i$. By substitution of this ansatz into the remaining terms we get

$$\begin{aligned} &\nu_{12} \int_{\mathbb{R}^d} (M_{12} - \bar{M}_1) \log \bar{M}_1 d\mathbf{v} + \nu_{21} \int_{\mathbb{R}^d} (M_{21} - \bar{M}_2) \log \bar{M}_2 d\mathbf{v} \\ &= \nu_{12} \int_{\mathbb{R}^d} (M_{12} - \bar{M}_1) \left[\log(n_1) + \frac{d}{2}\,\log\left(\frac{1}{2\,\pi\,T_1}\right) - \frac{|\mathbf{v} - \mathbf{u}_1|^2}{2\,T_1} \right] d\mathbf{v} \\ &+ \nu_{21} \int_{\mathbb{R}^d} (M_{21} - \bar{M}_2) \left[\log(n_2) + \frac{d}{2}\,\log\left(\frac{m}{2\,\pi\,T_2}\right) - \frac{m\,|\mathbf{v} - \mathbf{u}_2|^2}{2\,T_2} \right] d\mathbf{v} \\ &= \nu_{12}\, n_1 \left(-\frac{T_{12}}{T_1} - \frac{|\mathbf{u}_{12} - \mathbf{u}_1|^2}{2\,T_1} + 1 \right) + \nu_{21}\, n_2 \left(-\frac{T_{21}}{T_2} - \frac{m\,|\mathbf{u}_{21} - \mathbf{u}_2|^2}{2\,T_2} + 1 \right), \end{aligned}$$

that, taking into account the expressions (14) and (15) for the auxiliary parameters and recalling the relation (26), becomes

$$-\nu_{12}\, n_1\, b_{12}\, \frac{(T_1 - T_2)^2}{T_1\, T_2} - \left[\frac{\nu_{12}\, n_1}{T_1} \left(\gamma_{12} + \frac{(a_{12})^2}{2} \right) + \frac{\nu_{21}\, n_2}{T_2} \left(\gamma_{21} + \frac{(a_{21})^2}{2} \right) \right] |\mathbf{u}_1 - \mathbf{u}_2|^2;$$

this sum of negative terms vanishes if and only if $\mathbf{u}_1 = \mathbf{u}_2$ and $T_1 = T_2$, therefore the unique collision equilibrium admitted by our mixed Boltzmann–BGK model is $(F_1, F_2) = (M_1, M_2)$ provided in (16).

2.3. Hydrodynamic limits

Hydrodynamic equations may be derived from the kinetic model (12) in different collision dominated regimes [10]. In what follows we present the Euler equations corresponding to two different scaling hypothesis.

2.3.1. Case with all dominant collisions

We assume, as in classical hydrodynamic limits, that all mechanical collisions play a dominant role in the evolution. This is equivalent to set $\alpha = 1$ in the dimensionless kinetic system, hence obtaining

$$\begin{aligned} \frac{\partial f_1}{\partial t} + \mathbf{v} \cdot \nabla_{\mathbf{x}} f_1 &= \frac{1}{\varepsilon} Q_{11}(f_1, f_1) + \frac{1}{\varepsilon} \nu_{12} (M_{12} - f_1) \\ \frac{\partial f_2}{\partial t} + \mathbf{v} \cdot \nabla_{\mathbf{x}} f_2 &= \frac{1}{\varepsilon} \nu_{21} (M_{21} - f_2) + \frac{1}{\varepsilon} Q_{22}(f_2, f_2) , \end{aligned} \tag{28}$$

with ε representing a small parameter standing for the Knudsen number.

Collision invariants for the dominant terms (namely for the whole collision operator) correspond to species number densities n_1, n_2, global mass velocity $\mathbf{u}$ and global temperature T. Their evolution equations at Euler accuracy read as

$$\begin{aligned} &\frac{\partial n_1}{\partial t} + \nabla_{\mathbf{x}} \cdot (n_1 \, \mathbf{u}) = 0 , \\ &\frac{\partial n_2}{\partial t} + \nabla_{\mathbf{x}} \cdot (n_2 \, \mathbf{u}) = 0 , \\ &\frac{\partial}{\partial t}(\rho \mathbf{u}) + \nabla_{\mathbf{x}} \cdot (\rho \, \mathbf{u} \otimes \mathbf{u}) + \nabla_{\mathbf{x}} (n \, T) = \mathbf{0} , \\ &\frac{\partial}{\partial t} \left(\frac{1}{2} \rho |\mathbf{u}|^2 + \frac{d}{2} \, n \, T \right) + \nabla_{\mathbf{x}} \cdot \left[\left(\frac{1}{2} \rho |\mathbf{u}|^2 + \frac{d+2}{2} \, n \, T \right) \mathbf{u} \right] = 0 . \end{aligned} \tag{29}$$

Here, the total mass density ρ is given by $\rho = n_1 + m \, n_2$, since we have taken the particle mass of species 1 as reference value, therefore dimensionless masses are 1 and $m = m_2/m_1$, for species 1 and 2, respectively.

2.3.2. Case with dominant intraspecies collisions

We assume now that only resonant collisions, namely interactions involving a pair of particles of the same species, play the dominant role. This regime is well known to occur, for instance, in mixtures with constituents having very disparate masses [54, 39, 10]. More precisely, in our rescaled model we set $\alpha = \varepsilon$ and we get

$$\begin{aligned} \frac{\partial f_1}{\partial t} + \mathbf{v} \cdot \nabla_{\mathbf{x}} f_1 &= \frac{1}{\varepsilon} Q_{11}(f_1, f_1) + \nu_{12} (M_{12} - f_1) \\ \frac{\partial f_2}{\partial t} + \mathbf{v} \cdot \nabla_{\mathbf{x}} f_2 &= \nu_{21} (M_{21} - f_2) + \frac{1}{\varepsilon} Q_{22}(f_2, f_2) . \end{aligned} \tag{30}$$

Taking ε as small parameter, the dominant terms are the Boltzmann one–species operators. We apply the classical Chapman-Enskog method [23], and we expand each distribution function f_i in terms of the Knudsen number ε as $f_i = f_i^{(0)} + \varepsilon \, f_i^{(1)}$; consequently, similar expansions hold for macroscopic fields, but with the constraint (typical of the Chapman–Enskog procedure) of keeping unexpanded the collision invariants of the dominant part of the collision operators, that in the present regime are densities, mean velocities and temperatures of single species. From rescaled equations (30), at leading order we get

$$f_i^{(0)}(\mathbf{v}) = n_i \left(\frac{m_i}{2\pi T_i} \right)^{d/2} \exp\left(-\frac{m_i}{2T_i} |\mathbf{v} - \mathbf{u}_i|^2 \right) , \tag{31}$$

and Euler equations for n_i, $\mathbf{u}_i$, T_i ($i = 1, 2$) are thus provided by the zero–order terms of the weak form of kinetic equations (30)

$$\frac{\partial}{\partial t} \int_{\mathbb{R}^d} \phi_i(\mathbf{v}) \, f_i^{(0)} d\mathbf{v} + \nabla_{\mathbf{x}} \cdot \int_{\mathbb{R}^d} \phi_i(\mathbf{v}) \, \mathbf{v} \, f_i^{(0)} d\mathbf{v} = \nu_{ik}^{(0)} \int_{\mathbb{R}^d} \phi_i(\mathbf{v}) \left(M_{ik}^{(0)} - f_i^{(0)} \right) d\mathbf{v} \tag{32}$$

corresponding to the weight functions $\phi_i(\mathbf{v}) = 1,\, m_i\,\mathbf{v},\, \frac{1}{2}\,m_i\,|\mathbf{v}|^2$, with $(i,k) = (1,2)$ or $(2,1)$ and masses $m_1 = 1$ and $m_2 = m$ in our dimensionless frame. Notice that on the right hand sides the contributions due to the Boltzmann operators Q_{ii} (which would involve also the correction $f_i^{(1)}$) disappear because intra–species collisions do not modify mass, momentum and energy of the species itself. As expected, on the right sides there appear only suitable collisions contributions due to the interactions between the two different gases. The computations of streaming terms in (32) is usual in kinetic theory [22, 23], while we refer the interested reader to [10] for a detailed investigation of the collision contributions. Skipping intermediate details, the sought evolution equations may be cast as

$$
\begin{aligned}
&\frac{\partial n_1}{\partial t} + \nabla_{\mathbf{x}} \cdot (n_1\,\mathbf{u}_1) = 0\,,\\
&\frac{\partial n_2}{\partial t} + \nabla_{\mathbf{x}} \cdot (n_2\,\mathbf{u}_2) = 0\,,\\
&\frac{\partial}{\partial t}(n_1\mathbf{u}_1) + \nabla_{\mathbf{x}} \cdot (n_1\,\mathbf{u}_1 \otimes \mathbf{u}_1) + \nabla_{\mathbf{x}}(n_1\,T_1) = -\,\mu\,n_1\,n_2\,\frac{m}{1+m}\,(\mathbf{u}_1 - \mathbf{u}_2)\,,\\
&\frac{\partial}{\partial t}(m\,n_2\mathbf{u}_2) + \nabla_{\mathbf{x}} \cdot (m\,n_2\,\mathbf{u}_2 \otimes \mathbf{u}_2) + \nabla_{\mathbf{x}}(n_2\,T_2) = -\,\mu\,n_1\,n_2\,\frac{m}{1+m}\,(\mathbf{u}_2 - \mathbf{u}_1)\,,\\
&\frac{\partial}{\partial t}\left(\frac{1}{2}\,n_1\,|\mathbf{u}_1|^2 + \frac{d}{2}\,n_1\,T_1\right) + \nabla_{\mathbf{x}} \cdot \left[\left(\frac{1}{2}\,n_1|\mathbf{u}_1|^2 + \frac{d+2}{2}\,n_1\,T_1\right)\mathbf{u}_1\right]\\
&\qquad = -\,\mu\,n_1\,n_2\,\frac{m}{(1+m)^2}\left[(\mathbf{u}_1 + m\,\mathbf{u}_2)\cdot(\mathbf{u}_1 - \mathbf{u}_2) + d\,(T_1 - T_2)\right],\\
&\frac{\partial}{\partial t}\left(\frac{1}{2}\,m\,n_2\,|\mathbf{u}_2|^2 + \frac{d}{2}\,n_2\,T_2\right) + \nabla_{\mathbf{x}} \cdot \left[\left(\frac{1}{2}\,m\,n_2|\mathbf{u}_2|^2 + \frac{d+2}{2}\,n_2\,T_2\right)\mathbf{u}_2\right]\\
&\qquad = -\,\mu\,n_1\,n_2\,\frac{m}{(1+m)^2}\left[(\mathbf{u}_1 + m\,\mathbf{u}_2)\cdot(\mathbf{u}_2 - \mathbf{u}_1) + d\,(T_2 - T_1)\right].
\end{aligned}
\tag{33}
$$

Recalling that collision frequencies are provided by $\nu_{12} = n_2\,\mu$ and $\nu_{21} = n_1\,\mu$, we note that in the limit $\mu \to +\infty$ we recover $\mathbf{u}_1 = \mathbf{u}_2$ and $T_1 = T_2$, therefore equations (33) correctly reduce to classical Euler equations (29) relevant to situations in which all collisions are dominant.

3. The numerical scheme

In this section, we describe the numerical method designed to solve the dimensionless model (12). To make notation easier and less heavy in the fully discrete numerical scheme, we slightly change the notation of the Boltzmann collision operators in (12) as follows:

$$
Q_{11}(f_1, f_1) := Q(f_1), \qquad Q_{22}(f_2, f_2) := Q(f_2). \tag{34}
$$

For the sake of clarity we divide the discussion in different parts, each of them taking into account a specific description of the discretization. We start by discussing discrete ordinate methods for our kinetic model, we continue by introducing finite volume technique for the discrete ordinate model and we close our discussion with the time integration. A last part is dedicated to the study of the numerical method for what concerns its limit behaviors and the consistency with the hydrodynamic equations. We do not discuss here the spectral approximation of the collision operators $Q(f_1)$ and $Q(f_2)$, and we refer to [52, 37] for details about this technique in general and to [19] for an application in our context.

3.1. The Discrete Velocity Models (DVM)

We consider the following discrete space in velocity $\mathbf{v} = (v_{x_1},\, v_{x_2})$ with $\mathbf{x} = (x_1,\, x_2)$:

$$
\mathcal{V} = \{\mathbf{v}_{(k_1,k_2)} = (k_1\Delta v_{x_1} + v_{x_1,min},\, k_2\Delta v_{x_2} + v_{x_2,min})\,\}\,, \tag{35}
$$

with the mesh spacing in directions (x_1, x_2) given by

$$\Delta v_{x_1} = \frac{(v_{x_1,max} - v_{x_1,min})}{N_{x_1}}, \ \Delta v_{x_2} = \frac{(v_{x_2,max} - v_{x_2,min})}{N_{x_2}}. \tag{36}$$

The terms $\mathbf{v}_{min} = (v_{x_1,min}, v_{x_2,min})$ is the vector indicating the lower admissible velocity and $\mathbf{v}_{max} = (v_{x_1,max}, v_{x_2,max})$ the maximum one. In the following, for simplicity and to shorten the notation, we introduce the mono-index k, which spans all the discrete space of $N = N_{x_1} \times N_{x_2}$ total elements, i.e. the discrete velocity will be denoted by $\mathbf{v}_k$, $k = 1, \dots, N$. Furthermore, a regular Cartesian grid is assumed, hence implying that the mesh spacing is uniform, i.e. $\Delta v_{x_1} = \Delta v_{x_2} := \Delta v$.

The continuous distribution functions f_1 and f_2 are then replaced by the vectors $f_{1,\mathcal{K}}(\mathbf{x}, t)$ and $f_{2,\mathcal{K}}(\mathbf{x}, t)$ of size N and we assume that

$$\begin{aligned} f_{1,\mathcal{K}}(\mathbf{x}, t) &= (f_{1,k}(\mathbf{x}, t))_k, \qquad & f_{1,k}(\mathbf{x}, t) &\approx f_1(\mathbf{x}, \mathbf{v}_k, t), \\ f_{2,\mathcal{K}}(\mathbf{x}, t) &= (f_{2,k}(\mathbf{x}, t))_k, \qquad & f_{2,k}(\mathbf{x}, t) &\approx f_2(\mathbf{x}, \mathbf{v}_k, t). \end{aligned} \tag{37}$$

The truncation of the velocity space leads to loss of conservation because in general the support of the distribution functions is non compact, as for the case of the Maxwellian equilibrium states $M_{11}, M_{12}, M_{21}, M_{22}$. Nevertheless, taking sufficiently large bounds in velocity makes the loss of conservation negligible. We do not further discuss this issue here and we refer to previous works in which this problem has been tackled [40, 51]. We only observe that the scheme described in the sequel can be easily adapted to exactly match the moments of the distributions, if required.

The discrete ordinate (or velocity) kinetic model (DVM) consists then in the following coupled linear hyperbolic systems, each one composed of N equations which are linked through strongly nonlinear terms on the right hand side characterizing the collisions among equal and different species particles. Thus, we have

$$\partial_t f_{1,k} + \mathbf{v}_k \cdot \nabla_{\mathbf{x}} f_{1,k} = \tfrac{1}{\varepsilon} Q_k(f_{1,\mathcal{K}}) + \tfrac{\alpha}{\varepsilon} \nu_{12} \left(\mathcal{E}_{12,k}[U_1, U_2] - f_{1,k}\right), \quad k = 1, \dots, N \tag{38}$$

$$\partial_t f_{2,k} + \mathbf{v}_k \cdot \nabla_{\mathbf{x}} f_{2,k} = \tfrac{\alpha}{\varepsilon} \nu_{21} \left(\mathcal{E}_{21,k}[U_1, U_2] - f_{2,k}\right) + \tfrac{1}{\varepsilon} Q_k(f_{2,\mathcal{K}}), \quad k = 1, \dots, N, \tag{39}$$

where $\mathcal{E}_{12,k}[U_1, U_2]$ and $\mathcal{E}_{21,k}[U_1, U_2]$ represent suitable approximations of M_{12} and M_{21}. In practice we consider

$$\mathcal{E}_{12,k}[U_1, U_2] = M_{12}(\mathbf{x}, \mathbf{v}_k, t), \quad \mathcal{E}_{21,k}[U_1, U_2] = M_{21}(\mathbf{x}, \mathbf{v}_k, t), \tag{40}$$

and we define the vectors of the macroscopic quantities as

$$U_1 = (\rho_1, \rho_1 \mathbf{u}_1, E_1)^T, \quad U_2 = (\rho_2, \rho_2 \mathbf{u}_2, E_2)^T, \tag{41}$$

with $E_1 = \frac{1}{2} n_1 |\mathbf{u}_1|^2 + \frac{d}{2} n_1 T_1$ and $E_2 = \frac{1}{2} m n_2 |\mathbf{u}_2|^2 + \frac{d}{2} n_2 T_2$. These macroscopic quantities are obtained starting from the distribution functions $f_{1\mathcal{K}}(\mathbf{x}, t), f_{2\mathcal{K}}(\mathbf{x}, t)$ thanks to numerical integration in the phase space. In practice, we use these formulas

$$U_1 = \sum_{k=1}^{N} \Delta v^2 \, \phi_k f_{1,k} = \langle \phi_k f_{1,k} \rangle, \quad U_2 = \sum_{k=1}^{N} \Delta v^2 \, \phi_k f_{2,k} = \langle \phi_k f_{2,k} \rangle \tag{42}$$

with $\phi_k = (1, \mathbf{v}_k, |\mathbf{v}_k|^2)$. An analogous definition is used for the one–species Maxwellian distributions:

$$\mathcal{E}_{11,k}[U_1] = M_{11}(\mathbf{x}, \mathbf{v}_k, t), \quad \mathcal{E}_{22,k}[U_2] = M_{22}(\mathbf{x}, \mathbf{v}_k, t). \tag{43}$$

Finally, $Q_k(f_{1,\mathcal{K}})$ and $Q_k(f_{2,\mathcal{K}})$ appearing in (38) and (39) correspond to the solution given by a suitable spectral approximation of the collision integrals projected over the discrete velocity space $\mathcal{V}$. We briefly discuss this strategy in the following and we refer to [37] and [19] for details.

The collision operator modifies the solution only for what concerns the velocity variable and consequently the spectral method is applied only to that variable. We then restrict ourselves for a moment to consider simply $f_1 = f_1(\mathbf{v})$ and $f_2 = f_2(\mathbf{v})$. Moreover, the method applies to the continuous case and not to the discrete one and so, once the spectral approximation is derived, the solution is projected over the discrete ordinate space $\mathcal{V}$, this give $Q_k(f_{1,\mathcal{K}})$ and $Q_k(f_{2,\mathcal{K}})$ in formulas (38) and (39).

To proceed towards the approximation of the collision operators, we expand both f_1 and f_2 in Fourier and we denote by f_{1,N_M} and f_{2,N_M} the approximate functions

$$f_{1,N_M}(\mathbf{v}) = \sum_{k_1,k_2=-N_M}^{N_M} \hat{f}_{1,k} e^{ik\cdot\mathbf{v}} = \sum_{k=-N_M}^{N_M} \hat{f}_{1,k} e^{ik\cdot\mathbf{v}},\ f_{2,N_M}(\mathbf{v}) = \sum_{k_1,k_2=-N_M}^{N_M} \hat{f}_{2,k} e^{ik\cdot\mathbf{v}} = \sum_{k=-N_M}^{N_M} \hat{f}_{2,k} e^{ik\cdot\mathbf{v}} \tag{44}$$

with coefficients

$$\hat{f}_{1,k} = \frac{1}{(2\pi)^2} \int_{[-\pi,\pi]^2} f_1(\mathbf{v}) e^{-ik\cdot\mathbf{v}}\, d\mathbf{v},\ \hat{f}_{2,k} = \frac{1}{(2\pi)^2} \int_{[-\pi,\pi]^2} f_2(\mathbf{v}) e^{-ik\cdot\mathbf{v}}\, d\mathbf{v} \tag{45}$$

where N_M are the modes. Plugging the spectral expansions into the Boltzmann operators give

$$\hat{Q}_k(f_1) = \sum_{\substack{l,m=-N_M \\ l+m=k}}^{N_M} \hat{\beta}_F(l,m)\, \hat{f}_{1,l}\, \hat{f}_{1,m}, \quad \hat{Q}_k(f_2) = \sum_{\substack{l,m=-N_M \\ l+m=k}}^{N_M} \hat{\beta}_F(l,m)\, \hat{f}_{2,l}\, \hat{f}_{2,m}, \ \ k = -N_M, \dots, N_M, \tag{46}$$

with the coefficients $\hat{\beta}_F(l,m)$ which do not depend upon the distribution functions $f_{1,N_M}(\mathbf{v})$ and $f_{2,N_M}(\mathbf{v})$. These can be efficiently computed by resorting to the so-called Carlemann representation of the Boltzmann collision operator [37]. Finally, this representation permits to reduce (46) to a sum of convolution terms which in turns permits a fast evaluation of the Boltzmann operators. It has been shown in [37] that this algorithm uses $O(A\, N_M^2 \log_2 N_M^2)$ operations with A the number of discrete collision angles through the use of the fast Fourier techniques. Once $\hat{Q}_k(f_1)$ and $\hat{Q}_k(f_2)$ are computed by reversing back to the physical variable one easily get $Q_k(f_{1,\mathcal{K}})$ and $Q_k(f_{2,\mathcal{K}})$.

3.2. Space discretization

We detail here how the construction of the mesh in the physical two-dimensional domain Ω is realized. Arbitrarily shaped Voronoi-type meshes with a tessellation of N_P non-overlapping polygons $P_i, i = 1, \dots, N_P$ are considered. This is obtained starting from a Delaunay triangulation with N_T triangles and vertexes $\mathbf{x}_{c_i}, i = 1, \dots, N_P$ which are then used to generate the mesh employed in the computation. Inside each triangular element $T_j, j = 1, \dots, N_T$, we arbitrarily choose a point of coordinates $\mathbf{x}_{p_j}$ representing one of the vertices of the polygonal control volumes. Once the set of points $\mathbf{x}_{p_j}$ is fixed, then each element P_i is constructed by connecting the surrounding points $\mathbf{x}_{p_j} \in I_{c_i}$ having the generator point $\mathbf{x}_{c_i}$ as a vertex, see Figure 1. In other words, I_{c_i} is the set of the Voronoi neighborhood on the triangular mesh for the vertex located at $\mathbf{x}_{c_i}$. For example, if $\mathbf{x}_{p_j}$ is chosen as the center of mass of element T_j, then a rigorous Voronoi tessellation is retrieved. Different choices for the points $\mathbf{x}_{p_j}$ give instead arbitrarily meshes. The center of mass $\mathbf{x}_{m_i}$ of the obtained polygon P_i is computed by

$$\mathbf{x}_{m_i} = \frac{1}{|P_i|} \int_{P_i} \mathbf{x}\, d\mathbf{x}. \tag{47}$$

Let now N_{V_i} denote the number of vertexes of polygon P_i, i.e the number of points $\mathbf{x}_{p_j}$ belonging to each set $I_{c_i}, c_i = 1, \dots, N_P$. In order to be able to numerically integrate any quantity inside the cell P_i, we divide the polygon P_i in N_{V_i} triangles by connecting the points $\mathbf{x}_{m_i}$, i.e. the centroid, with each vertex of I_{c_i}. Thus integration is performed by Gauss formulae of suitable order of accuracy [55] over each sub-triangle. This sub-triangulation is referred to as $\mathcal{T}(P_i)$ in the following, and it is highlighted in blue in Figure 1.

3.2.1. Central WENO reconstruction on polygonal meshes

In this part we discuss the high order polynomial reconstruction starting from the following cell averages at time t^n

$$\bar{f}^n_{1,k,i} = \frac{1}{|P_i|} \int_{P_i} f_{1,k}(\mathbf{x}, t^n) d\mathbf{x}, \qquad \bar{f}^n_{2,k,i} = \frac{1}{|P_i|} \int_{P_i} f_{2,k}(\mathbf{x}, t^n) d\mathbf{x}. \tag{48}$$

These values are computed for each discrete velocity $k = 1, \dots, N$ and in each spatial cell $\mathbf{x} \in P_i,\ i \in [1, N_P]$ with $|P_i|$ the surface of cell P_i. In the sequel, for compactness of the notation, we will also make use of the quantities $\bar{f}^n_{1,i}, \bar{f}^n_{2,i}$ which read

$$\bar{f}^n_{1,i} = (\bar{f}^n_{1,1,i}, \dots, \bar{f}^n_{1,N,i}), \qquad \bar{f}^n_{2,i} = (\bar{f}^n_{2,1,i}, \dots, \bar{f}^n_{2,N,i}), \tag{49}$$

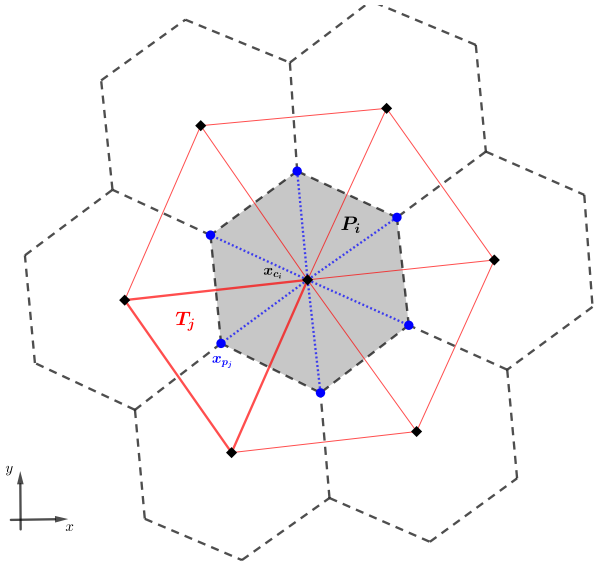

Figure 1: Example of mesh realization. The black dotted lines indicates the perimeters of the elements $P_j,\ j = 1, \dots, N_p$. The element P_i is in gray while the Delaunay triangulation used to construct this element is in red solid line. The generator points $\mathbf{x}_{c_i}$ as well as the points $\mathbf{x}_{p_j}$ chosen inside each triangle T_k are shown. The triangulation used to numerically integrate the variables in the finite volume method is identified by the dotted blue lines.

i.e. the vectors containing the information relative to the distribution functions in each control volume P_i. The Central WENO reconstructions of the functions $f_1(\mathbf{x}, \mathbf{v}_k, t)$, $f_2(\mathbf{x}, \mathbf{v}_k, t)$ from the cell averages $\bar{f}^n_{1,k,i}$, $\bar{f}^n_{2,k,i}$ which we are going to describe will be addressed with $f^{W,n}_{1,k,i}(\mathbf{x})$, $f^{W,n}_{2,k,i}(\mathbf{x})$ in the rest of the paper. In the following, we detail such reconstruction in the sole case of $f_1(\mathbf{x}, \mathbf{v}_k, t)$, being the reconstruction for $f_2(\mathbf{x}, \mathbf{v}_k, t)$ analogous.

A non-oscillatory high order polynomial function approximating the cell average quantities is obtained in two steps. The first one consists in computing a polynomial function $f_{1,opt,k,i}(\mathbf{x})$ of degree $M > 1$ for every cell P_i. The second one consists in combining this function $f_{1,opt,k,i}(\mathbf{x})$ with a set of first order polynomials, which are consequently non-oscillatory, and to construct a nonlinear combination of this family of functions with the scope of having both high accuracy and monotonicity. The polynomial $f_{1,opt,k,i}(\mathbf{x})$ relative to a stencil $\tilde{\mathcal{S}}_i$, containing the cell P_i and a set of close neighbors, is obtained as the solution of

$$f_{1,opt,k,i}(\mathbf{x}) = \underset{p \in \mathcal{P}_i}{\operatorname{argmin}} \sum_{P_j \in \tilde{\mathcal{S}}_i} \left(\bar{f}^n_{1,k,j} - \frac{1}{|P_j|} \int_{P_j} p(\mathbf{x}) d\mathbf{x} \right)^2, \tag{50}$$

where $\mathcal{P}_i$ is the set of all polynomial functions $\mathbb{P}_M$ of degree at most M, satisfying

$$\mathcal{P}_i = \left\{ p \in \mathbb{P}_M : \bar{f}^n_{1,k,i} = \frac{1}{|P_i|} \int_{P_i} p(\mathbf{x}) d\mathbf{x} \right\} \subset \mathbb{P}_M. \tag{51}$$

The meaning of the above relation is clear: $f_{1,opt,k,i}(\mathbf{x})$ is the polynomial of degree M taking the value $\bar{f}^n_{1,k,i}$ in the center of cell P_i and close in the L^2 sense to the neighbor cell averages, the ones in the stencil $\tilde{\mathcal{S}}_i$. We remark that even if the number of degrees of freedom, and so the number of cell averages, needed to compute $f_{1,opt,k,i}(\mathbf{x})$ is $(M+1)(M+2)/2$, a larger set of points must in general be considered to construct such interpolation to avoid ill-posedness which may be due to the unstructured nature of the mesh (see [7] for details).

We now define a set of degree one polynomials using the cell P_i and other two cells. We indicate by $f^s_{1,p,k,i}(\mathbf{x})$ the linear polynomial belonging to this set with $s = 1, \dots, N_{V_i}$ and N_{V_i} the number of polynomials. To conclude the

construction, we define a so-called *central* polynomial $f^0_{1,p,k,i}(\mathbf{x})$ by subtraction, i.e.

$$f^0_{1,p,k,i}(\mathbf{x}) = \frac{1}{\lambda_{0,i}}\left(f_{1,opt,k,i}(\mathbf{x}) - \sum_{s=1}^{N_{V_i}} \lambda_{s,i} f^s_{1,p,k,i}(\mathbf{x})\right) \in \mathbb{P}_M, \tag{52}$$

where the coefficients $\lambda_{0,i}, \ldots, \lambda_{N_{V_i},i}$ are positive and such that $\lambda_{0,i} \gg \lambda_{s,i}$ with $s = 1, \ldots, N_{V_i}$ and $\sum_{s=0}^{N_{V_i}} \lambda_{s,i} = 1$. The CWENO function $f^{W,n}_{1,k,i}(\mathbf{x})$ is finally obtained through a nonlinear combination reading

$$f^{1,W,n}_{k,i}(\mathbf{x}) = \sum_{s=0}^{N_{V_i}} \omega_{s,k,i}\, f^s_{1,p,k,i}(\mathbf{x}), \tag{53}$$

where $\omega_{s,k,i}$ are non linear weights given by

$$\omega_{s,k,i} = \frac{\tilde{\omega}_{s,k,i}}{\sum_{s=0}^{N_{V_i}} \tilde{\omega}_{s,k,i}}, \qquad \text{with} \qquad \tilde{\omega}_{s,k,i} = \frac{\lambda_{s,i}}{(\sigma_{s,k,i} + \epsilon)^r}, \tag{54}$$

with ϵ and r being parameters chosen as done in [38]. The coefficients $\sigma_{s,k,i}$ are the indicators which permits to avoid the oscillations and are defined as classically done in WENO reconstruction, see [19] for details. In the above detailed reconstruction procedure the integrals appearing are computed by Gauss formulae summing the contribution of each triangle $T_j \in \mathcal{T}(P_i)$ composing the cell P_i [55].

The same reconstruction holds for the distribution function relative to the second species $f^{2,W,n}_{k,i}(\mathbf{x})$. More in general, this operation could be applied to any given quantity defined as a cell average and, when performed, it will be addressed with superscript W to distinguish between the cell average and the corresponding CWENO reconstruction. In particular, in the sequel we will often refer to the polynomials $Q^W_{1,k}(\bar{f}^n_{1,i})(\mathbf{x})$ and $Q^W_{2,k}(\bar{f}^n_{2,i})(\mathbf{x})$, i.e. to the polynomial reconstructions of the Boltzmann operators computed in the cell centers.

3.2.2. Finite volume scheme on polygonal meshes

We move now a step back to equations (38) and (39) and we write a finite volume formulation for this coupled model obtaining for $k = 1, \ldots, N,\ i = 1, \ldots, N_P$

$$\begin{aligned}
\partial_t \int_{P_i} f_{1,k}\, d\mathbf{x} + \int_{P_i} \mathbf{v}_k \cdot \nabla_{\mathbf{x}} f_{1,k}\, d\mathbf{x} &= \frac{1}{\varepsilon}\int_{P_i} Q_{1,k}(f_{1,\mathcal{K}})\, d\mathbf{x} \\
&+ \frac{\alpha}{\varepsilon}\int_{P_i} \nu_{12}(\mathcal{E}_{12,k}[U_1, U_2] - f_{1,k})\, d\mathbf{x}, \qquad (55)\\
\partial_t \int_{P_i} f_{2,k}\, d\mathbf{x} + \int_{P_i} \mathbf{v}_k \cdot \nabla_{\mathbf{x}} f_{2,k}\, d\mathbf{x} &= \frac{\alpha}{\varepsilon}\int_{P_i} \nu_{21}(\mathcal{E}_{21,k}[U_1, U_2] - f_{2,k})\, d\mathbf{x} \\
&+ \frac{1}{\varepsilon}\int_{P_i} Q_{2,k}(f_{2,\mathcal{K}})\, d\mathbf{x}. \qquad (56)
\end{aligned}$$

Using the divergence theorem, we get for $k = 1, \ldots, N,\ i = 1, \ldots, N_P$,

$$\begin{aligned}
\partial_t \int_{P_i} f_{1,k}\, d\mathbf{x} &= -\sum_{j=1}^{N_{V_i}} \int_{\partial P_{ij}} L(f_{1,k}) \cdot\ \mathbf{n}_{ij}\, dS \\
&+ \frac{1}{\varepsilon}\int_{P_i} Q_{1,k}(f_{1,\mathcal{K}})\, d\mathbf{x} + \frac{\alpha}{\varepsilon}\int_{P_i} \nu_{12}(\mathcal{E}_{12,k}[U_1, U_2] - f_{1,k})\, d\mathbf{x}, \qquad (57)\\
\partial_t \int_{P_i} f_{2,k}\, d\mathbf{x} &= -\sum_{j=1}^{N_{V_i}} \int_{\partial P_{ij}} L(f_{2,k}) \cdot\ \mathbf{n}_{ij}\, dS \\
&+ \frac{\alpha}{\varepsilon}\int_{P_i} \nu_{21}(\mathcal{E}_{21,k}[U_1, U_2] - f_{2,k})\, d\mathbf{x} + \frac{1}{\varepsilon}\int_{P_i} Q_{2,k}(f_{2,\mathcal{K}})\, d\mathbf{x}. \qquad (58)
\end{aligned}$$

In the above system of equation, we have that $\mathbf{n}_{ij}$ is the unit vector normal to the boundary ∂P_i of element P_i. Moreover, we have that ∂P_{ij} is the line shared between element P_i and P_j. We also have that $L(f_{1,k}), L(f_{2,k})$ are the numerical flux functions $(\mathbf{v}_k f_{1,k})$ and $(\mathbf{v}_k f_{2,k})$. Starting from (57)-(58) we easily write a first order in time explicit method which reads:

$$\begin{aligned}
\bar{f}^{n+1}_{1,k,i} &= \bar{f}^{n}_{1,k,i} - \frac{\Delta t}{|P_i|}\sum_{j=1}^{N_{V_i}}\int_{\partial P_{ij}} L(\bar{f}^{n}_{1,k,i})\cdot\ \mathbf{n}_{ij}\, dS + \frac{\Delta t}{|P_i|}\int_{P_i} Q_{1,k}(\bar{f}^{n}_{1,i,\mathcal{K}})\, d\mathbf{x} \\
&+ \frac{1}{|P_i|}\frac{\alpha}{\varepsilon}\int_{P_i} \nu_{12}(\bar{\mathcal{E}}^{n}_{12,k,i}[U_1,U_2] - \bar{f}^{n}_{1,k,i})\, d\mathbf{x}, \qquad (59)\\
\bar{f}^{n+1}_{2,k,i} &= \bar{f}^{n}_{2,k,i} - \frac{\Delta t}{|P_i|}\sum_{j=1}^{N_{V_i}}\int_{\partial P_{ij}} L(\bar{f}^{n}_{2,k,i})\cdot\ \mathbf{n}_{ij}\, dS \\
&+ \frac{1}{|P_i|}\frac{\alpha}{\varepsilon}\int_{P_i} \nu_{21}(\bar{\mathcal{E}}^{n}_{21,k,i}[U_1,U_2] - \bar{f}^{n}_{2,k,i})\, d\mathbf{x} + \frac{\Delta t}{|P_i|}\int_{P_i} Q_{2,k}(\bar{f}^{n}_{2,i,\mathcal{K}})\, d\mathbf{x}, \qquad (60)
\end{aligned}$$

where the numerical fluxes are of Rusanov type. Now, by employing the CWENO reconstruction presented previously we substitute $\bar{f}^{n}_{1,k,i}$ by $f^{W,n}_{1,k,i}(\mathbf{x})$ and the same for $\bar{f}^{n}_{2,k,i}$ with $f^{W,n}_{2,k,i}(\mathbf{x})$. This permits an high order evaluation of the fluxes and of the collision terms. In the same way, the cell average Maxwellian functions and the cell average distribution function of the second species appearing in (59)-(60) may be substituted with high order in space reconstruction values and the same for what concerns the Boltzmann collision operators once the spectral method is used on the cell averages. Thus, the high order in space finite volume scheme reads for $k = 1,\dots,N, \quad i = 1,\dots,N_P$ as

$$\begin{aligned}
\bar{f}^{n+1}_{1,k,i} &= \bar{f}^{n}_{1,k,i} - \frac{\Delta t}{|P_i|}\sum_{j=1}^{N_{V_i}}\int_{\partial P_{ij}} L(f^{W,n}_{1,k,i}(\mathbf{x}))\cdot\ \mathbf{n}_{ij}\, dS \\
&+ \frac{\Delta t}{|P_i|}\int_{P_i} Q^{W}_{1,k}(\bar{f}^{n}_{1,i,\mathcal{K}})(\mathbf{x})\, d\mathbf{x} + \frac{1}{|P_i|}\frac{\alpha}{\varepsilon}\int_{P_i} \nu_{12}(\bar{\mathcal{E}}^{W,n}_{12,k,i}[U_1,U_2] - \bar{f}^{W,n}_{1,k,i})\, d\mathbf{x}, \qquad (61)\\
\bar{f}^{n+1}_{2,k,i} &= \bar{f}^{n}_{2,k,i} - \frac{\Delta t}{|P_i|}\sum_{j=1}^{N_{V_i}}\int_{\partial P_{ij}} L(f^{W,n}_{2,k,i}(\mathbf{x}))\cdot\ \mathbf{n}_{ij}\, dS \\
&+ \frac{1}{|P_i|}\frac{\alpha}{\varepsilon}\int_{P_i} \nu_{21}(\bar{\mathcal{E}}^{W,n}_{21,k,i}[U_1,U_2] - \bar{f}^{W,n}_{2,k,i})\, d\mathbf{x} + \frac{\Delta t}{|P_i|}\int_{P_i} Q^{W}_{2,k}(\bar{f}^{n}_{2,i,\mathcal{K}})(\mathbf{x})\, d\mathbf{x}. \qquad (62)
\end{aligned}$$

In order to improve the time accuracy and to have a method which is able to handle the different values of the Knudsen number ε without time step limitations, in the next section, we introduce a particular class of high order time discretizations which enjoy the property of being stable independently on the value of the relaxation parameter ε.

3.3. Time Discretization

We present here the time discretization technique employed in our numerical method. This takes inspiration from the class of Implicit-Explicit (IMEX) methods [3, 29] which are used to handle the different scales present in the model. In particular, we deal with three different regimes. The first one is the rarefied regime in which all collisions act at the same pace as the transport scale. The second one arrives when all collisions are dominant giving rise to a standard compressible Euler model for two species with the same mean velocity and temperature. This limit model has been shortly reported and discussed in Section 2.3.1. The third case is the so-called resonant collisions regime presented in Section 2.3.2, in which interactions involving pair of particles of the same species play the dominant role. In this latter situation, the corresponding macroscopic equations describe a fluid with two interacting phases where, however, each species has its distinct mean velocity and temperature field.

In order to be able to capture these different regimes with the same numerical method, the same accuracy and using the same time step Δt, we introduce a specific type of IMEX Runge-Kutta methods belonging to the class of asymptotic-preserving (AP) schemes [30, 26, 27, 46]. In particular, we consider the extension, for the first time up to our knowledge, to multispecies kinetic equations of the schemes introduced and theoretically analyzed in [28, 29] and

used in [19] in a finite volume setting. After the introduction of the methods, in the next Section 3.4, we study their asymptotic properties. Starting from equation (57)-(58), we introduce the following general formulation

$$\begin{aligned}
\bar{F}^{(l)}_{1,k,i} &= \bar{f}^{n}_{1,k,i} - \Delta t \sum_{m=1}^{l-1} \tilde{a}_{lm} \langle L(F^{W,(m)}_{1,k,i}) \rangle_{\mathbf{x}} + \frac{\Delta t}{\varepsilon} \sum_{m=1}^{l} a_{lm} \langle Q^{W}_{1,k}(\bar{F}^{(m)}_{1,i,\mathcal{K}}) \rangle_{\mathbf{x}} \\
&+ \frac{\Delta t \alpha}{\varepsilon} \sum_{m=1}^{l} a_{lm} \langle Q^{W}_{BGK_{1,2},k}(\bar{U}_{1,i}, \bar{U}_{2,i}, \bar{F}^{(m)}_{1,i,\mathcal{K}}) \rangle_{\mathbf{x}} \qquad (63) \\
\bar{f}^{n+1}_{1,k,i} &= \bar{f}^{n}_{1,k,i} - \Delta t \sum_{m=1}^{\iota} \tilde{w}_{m} \langle L(F^{W,(m)}_{1,k,i}) \rangle_{\mathbf{x}} + \frac{\Delta t}{\varepsilon} \sum_{m=1}^{\iota} w_{m} \langle Q^{W}_{1,k}(\bar{F}^{(m)}_{1,i,\mathcal{K}}) \rangle_{\mathbf{x}} \\
&+ \frac{\Delta t \alpha}{\varepsilon} \sum_{m=1}^{\iota} w_{m} \langle Q^{W}_{BGK_{1,2},k}(\bar{U}_{1,i}, \bar{U}_{2,i}, \bar{F}^{(m)}_{1,i,\mathcal{K}}) \rangle_{\mathbf{x}} \qquad (64) \\
\bar{F}^{(l)}_{2,k,i} &= \bar{f}^{n}_{2,k,i} - \Delta t \sum_{m=1}^{l-1} \tilde{a}_{lm} \langle L(F^{W,(m)}_{2,k,i}) \rangle_{\mathbf{x}} + \frac{\Delta t}{\varepsilon} \sum_{m=1}^{l} a_{lm} \langle Q^{W}_{2,k}(\bar{F}^{(m)}_{2,i,\mathcal{K}}) \rangle_{\mathbf{x}} \\
&+ \frac{\Delta t \alpha}{\varepsilon} \sum_{m=1}^{l} a_{lm} \langle Q^{W}_{BGK_{2,1},k}(\bar{U}_{1,i}, \bar{U}_{2,i}, \bar{F}^{(m)}_{2,i,\mathcal{K}}) \rangle_{\mathbf{x}} \qquad (65) \\
\bar{f}^{n+1}_{2,k,i} &= \bar{f}^{n}_{2,k,i} - \Delta t \sum_{m=1}^{\iota} \tilde{w}_{m} \langle L(F^{W,(m)}_{2,k,i}) \rangle_{\mathbf{x}} + \frac{\Delta t}{\varepsilon} \sum_{m=1}^{\iota} w_{m} \langle Q^{W}_{2,k}(\bar{F}^{(m)}_{2,i,\mathcal{K}}) \rangle_{\mathbf{x}} \\
&+ \frac{\Delta t \alpha}{\varepsilon} \sum_{m=1}^{\iota} w_{m} \langle Q^{W}_{BGK_{2,1},k}(\bar{U}_{1,i}, \bar{U}_{2,i}, \bar{F}^{(m)}_{2,i,\mathcal{K}}) \rangle_{\mathbf{x}} \qquad (66)
\end{aligned}$$

In the above expression, $\bar{U}_{1,i}$ and $\bar{U}_{2,i}$ are the cell averages of the macroscopic quantities related to each species in the control volume P_i, according to the definition (41). A total number of ι stages builds the underlying Runge-Kutta time discretization. The functions $\bar{F}^{(l)}_{1,k,i}$ and $\bar{F}^{(l)}_{2,k,i}$ given by (63) and (65) are the so-called stage values of the Runge-Kutta method which are used to identify the numerical solution at different time levels between $[t^n, t^{n+1}]$. Using the same notation, $F^{W,(m)}_{1,k,i}(\mathbf{x})$ and $F^{W,(m)}_{2,k,i}(\mathbf{x})$ represent the high order CWENO reconstruction of the stage value (m) obtained following the algorithm outlined in Section 3.2.1. Using these values, it is possible to compute the quantities

$$\langle L(F^{W,(l)}_{1,k,i}) \rangle_{\mathbf{x}} = \frac{1}{|P_i|} \sum_{j=1}^{N_{V_i}} \int_{\partial P_{ij}} L(F^{W,(l)}_{1,k,i}(\mathbf{x})) \cdot \mathbf{n}_{ij} \, dS = L^{W,(l)}_{1,k,i}, \qquad (67)$$

$$\langle L(F^{W,(l)}_{2,k,i}) \rangle_{\mathbf{x}} = \frac{1}{|P_i|} \sum_{j=1}^{N_{V_i}} \int_{\partial P_{ij}} L(F^{W,(l)}_{2,k,i}(\mathbf{x})) \cdot \mathbf{n}_{ij} \, dS = L^{W,(l)}_{2,k,i}, \qquad (68)$$

and

$$\langle Q^{W}_{1,k}(\bar{F}^{(l)}_{1,i,\mathcal{K}}) \rangle_{\mathbf{x}} = \frac{1}{|P_i|} \int_{P_i} Q^{W}_{1,k}(\bar{F}^{(l)}_{1,i,\mathcal{K}})(\mathbf{x}) \, d\mathbf{x} = Q^{W,(l)}_{1,k}, \qquad (69)$$

$$\langle Q^{W}_{1,k}(\bar{F}^{(l)}_{2,i,\mathcal{K}}) \rangle_{\mathbf{x}} = \frac{1}{|P_i|} \int_{P_i} Q^{W}_{2,k}(\bar{F}^{(l)}_{2,i,\mathcal{K}})(\mathbf{x}) \, d\mathbf{x} = Q^{W,(l)}_{2,k}. \qquad (70)$$

Finally, relying on suitable Gauss quadrature formula, one can evaluate the following quantities

$$\begin{aligned}
Q^{W}_{BGK_{1,2},k}(\bar{U}_{1,i}, \bar{U}_{2,i}, \bar{F}^{(l)}_{1,i,\mathcal{K}}) &= \nu_{12}(\mathcal{E}^{W,n}_{12,k,i}[\bar{U}_1, \bar{U}_2] - F^{W,(l)}_{1,i,k}), \\
Q^{W}_{BGK_{2,1},k}(\bar{U}_{1,i}, \bar{U}_{2,i}, \bar{F}^{(m)}_{2,i,\mathcal{K}}) &= \nu_{21}(\mathcal{E}^{W,n}_{21,k,i}[\bar{U}_1, \bar{U}_2] - F^{W,(l)}_{2,i,k}), \qquad (71)
\end{aligned}$$

and the corresponding integrals

$$\langle Q^{W}_{BGK_{1,2},k}(\bar{U}_{1,i}, \bar{U}_{2,i}, \bar{F}^{(m)}_{1,i,\mathcal{K}}) \rangle_{\mathbf{x}} = \frac{1}{|P_i|} \int_{P_i} Q^{W}_{BGK_{1,2},k}(\bar{U}_{1,i}, \bar{U}_{2,i}, \bar{F}^{(m)}_{1,i,\mathcal{K}})(\mathbf{x}) \, d\mathbf{x}, \qquad (72)$$

$$\langle Q^W_{BGK_{2,1},k}(\bar{U}_{1,i},\bar{U}_{2,i},\bar{F}^{(m)}_{2,i,\mathcal{K}})\rangle_{\mathbf{x}} = \frac{1}{|P_i|}\int_{P_i} Q^W_{BGK_{2,1},k}(\bar{U}_{1,i},\bar{U}_{2,i},\bar{F}^{(m)}_{2,i,\mathcal{K}})(\mathbf{x})\,d\mathbf{x}. \tag{73}$$

To have a perfectly defined scheme it remains to define the role of the coefficients $\tilde{a}_{lm}$ and a_{lm} in (63)-(66) which are used to characterize the explicit and the (diagonally) implicit Runge-Kutta method, together with the vectors $\tilde{w} = (\tilde{w}_1,\dots,\tilde{w}_\iota)^T$ and $w = (w_1,\dots,w_\iota)^T$. The coefficients of an IMEX method are typically given using a double Butcher tableau, see Table 1, where $\tilde{c}_l = \sum_{m=1}^{l-1}\tilde{a}_{lm}$, $c_l = \sum_{m=1}^{l} a_{lm}$. In particular, in the following, we rely on the so-called stiffly-accurate IMEX schemes, intending with such nomenclature that the coefficients of the last level of the scheme coincide with respectively the vectors $\tilde{w} = (\tilde{w}_1,\dots,\tilde{w}_\iota)^T$ and $w = (w_1,\dots,w_\iota)^T$. This means that for such methods the numerical solutions $\bar{f}^{n+1}_{1,k,i}, \bar{f}^{n+1}_{2,k,i}$ are equal to $\bar{F}^{(\iota)}_{1,k,i}, \bar{F}^{(\iota)}_{2,k,i}$ respectively. For the sole case of the BGK

Table 1: An example of the Butcher tableau for the explicit and implicit Runge-Kutta schemes of an IMEX discretization.

$\tilde{c}$	$\tilde{A}$
	$\tilde{w}^T$

c	A
	w^T

operator, we observe that the high order integration can be written as proposed in [18] as

$$\begin{aligned}\langle Q^W_{BGK_{1,2},k}(\bar{U}_{1,i},\bar{U}_{2,i},\bar{F}^{(m)}_{1,i,\mathcal{K}})\rangle_{\mathbf{x}} &= \frac{1}{|P_i|}\int_{P_i} Q^W_{BGK_{1,2},k}(\bar{U}_{1,i},\bar{U}_{2,i},\bar{F}^{(m)}_{1,i,\mathcal{K}})(\mathbf{x})\,d\mathbf{x}\\ &= \langle Q_{BGK_{1,2},k}(\bar{U}_{1,i},\bar{U}_{2,i},\bar{F}^{(m)}_{1,i,\mathcal{K}})\rangle_{\mathbf{x}} + O(h^2),\end{aligned} \tag{74}$$

where h is the typical mesh size (taken as the square root of the surface of the cell) and $\bar{F}^{(m)}_{1,i,\mathcal{K}}$, $\bar{U}_{1,i}, \bar{U}_{2,i}$ are the cell average quantities at the stage m. The interpretation of the above formula is clear: if one considers a second order in space method, the cell average can be used in the computation of the integrals appearing as source terms. Since in this work we restrict to the case of second order schemes, we replace in the following the integrals of the BGK operators $\langle Q^W_{BGK_{1,2},k}(\bar{U}_{1,i},\bar{U}_{2,i},\bar{F}^{(m)}_{1,i,\mathcal{K}})\rangle_{\mathbf{x}}$ and $\langle Q^W_{BGK_{2,1},k}(\bar{U}_{1,i},\bar{U}_{2,i},\bar{F}^{(m)}_{2,i,\mathcal{K}})\rangle_{\mathbf{x}}$ by the cell average and we use the short notation

$$Q^{(m)}_{BGK_{1,2},k} := \langle Q_{BGK_{1,2},k}(\bar{U}_{1,i},\bar{U}_{2,i},\bar{F}^{(m)}_{1,i,\mathcal{K}})\rangle_{\mathbf{x}}, \qquad Q^{(m)}_{BGK_{2,1},k} := \langle Q_{BGK_{2,1},k}(\bar{U}_{1,i},\bar{U}_{2,i},\bar{F}^{(m)}_{1,i,\mathcal{K}})\rangle_{\mathbf{x}}. \tag{75}$$

Unfortunately, the direct application of the time integration method above described is very difficult in practice. The inversion of the numerical discretization of the Boltzmann operators $Q^W_{1,k}(\bar{F}^{(m)}_{1,i,\mathcal{K}})$ and $Q^W_{2,k}(\bar{F}^{(m)}_{2,i,\mathcal{K}})$ would imply the solution of a very large non linear system at each stage of the Runge-Kutta time stepping and it has to be avoided. In order to bypass this issue we use a strategy proposed in [36]. The idea consists in using a penalization of the Boltzmann operator by a cell centered BGK operator relative to the single species dynamics. Thus, one first recasts equations (12) as

$$\begin{aligned}\frac{\partial f_1}{\partial t} + \mathbf{v}\cdot\nabla_{\mathbf{x}} f_1 &= G_P(f_1) + \frac{\nu_{11}}{\varepsilon}\,(M_{11} - f_1) + \frac{\alpha}{\varepsilon}\,\nu_{12}\,(M_{12} - f_1)\\ \frac{\partial f_2}{\partial t} + \mathbf{v}\cdot\nabla_{\mathbf{x}} f_2 &= \frac{\alpha}{\varepsilon}\,\nu_{21}\,(M_{21} - f_2) + G_P(f_2) + \frac{\nu_{22}}{\varepsilon}\,(M_{22} - f_2),\end{aligned} \tag{76}$$

where

$$G_P(f_1) = \frac{1}{\varepsilon}(Q(f_1) - \nu_{11}\,(M_{11} - f_1)), \qquad G_P(f_2) = \frac{1}{\varepsilon}(Q(f_2) - \nu_{22}\,(M_{22} - f_2)). \tag{77}$$

Successively, we use the implicit time discretization for the four BGK operators appearing in (76) while we keep the

penalization operators $G_P(f_1), G_P(f_2)$ explicit. The modified IMEX Runge-Kutta schemes become then

$$\begin{aligned}
\bar{F}^{(l)}_{1,k,i} &= \bar{f}^n_{1,k,i} - \Delta t \sum_{m=1}^{l-1} \tilde{a}_{lm} \left(L^{W,(m)}_{1,k,i} - G^{W,(m)}_{1,k,i} \right) + \frac{\Delta t}{\varepsilon} \sum_{m=1}^{l} a_{lm} Q^{(m)}_{BGK_{1,1},k} \\
&+ \frac{\Delta t \alpha}{\varepsilon} \sum_{m=1}^{l} a_{lm} Q^{(m)}_{BGK_{1,2},k} \qquad (78) \\
\bar{f}^{n+1}_{1,k,i} &= \bar{f}^n_{1,k,i} - \Delta t \sum_{m=1}^{\iota} \tilde{w}_m \left(L^{W,(m)}_{1,k,i} - G^{W,(m)}_{1,k,i} \right) + \frac{\Delta t}{\varepsilon} \sum_{m=1}^{\iota} w_m Q^{(m)}_{BGK_{1,1},k} \\
&+ \frac{\Delta t \alpha}{\varepsilon} \sum_{m=1}^{\iota} w_m Q^{(m)}_{BGK_{1,2},k} \qquad (79) \\
\bar{F}^{(l)}_{2,k,i} &= \bar{f}^n_{2,k,i} - \Delta t \sum_{m=1}^{l-1} \tilde{a}_{lm} \left(L^{W,(m)}_{2,k,i} - G^{W,(m)}_{2,k,i} \right) + \frac{\Delta t}{\varepsilon} \sum_{m=1}^{l} a_{lm} Q^{(m)}_{BGK_{2,2},k} \\
&+ \frac{\Delta t \alpha}{\varepsilon} \sum_{m=1}^{l} a_{lm} Q^{(m)}_{BGK_{2,1},k} \qquad (80) \\
\bar{f}^{n+1}_{2,k,i} &= \bar{f}^n_{2,k,i} - \Delta t \sum_{m=1}^{\iota} \tilde{w}_m \left(L^{W,(m)}_{2,k,i} - G^{W,(m)}_{2,k,i} \right) + \frac{\Delta t}{\varepsilon} \sum_{m=1}^{\iota} w_m Q^{(m)}_{BGK_{2,2},k} \\
&+ \frac{\Delta t \alpha}{\varepsilon} \sum_{m=1}^{\iota} w_m Q^{(m)}_{BGK_{2,1},k} \qquad (81)
\end{aligned}$$

where

$$G^{W,(m)}_{1,k,i} = \tfrac{1}{\varepsilon} \left(Q^{W,(m)}_{1,k} - Q^{(m)}_{BGK_{11},k} \right), \qquad (82)$$

$$G^{W,(m)}_{2,k,i} = \tfrac{1}{\varepsilon} \left(Q^{W,(m)}_{2,k} - Q^{(m)}_{BGK_{22},k} \right) \qquad (83)$$

where the quantities $Q^{(m)}_{BGK_{11},k}, Q^{(m)}_{BGK_{22},k}$ are the second order in space integrals of the one species BGK operators. Now, thanks to the implicit treatment of the possibly stiff collision operators, the time step Δt is computed according to a CFL-type stability condition which only depends on the hyperbolic transport term, that is

$$\Delta t = \mathrm{CFL} \left(\frac{\min_\Omega h_i}{\max_{\mathcal{K}}(|\mathbf{v}_k|)} \right), \qquad \mathrm{CFL} = \frac{1}{2}, \qquad (84)$$

with the characteristic mesh size $h_i = \sqrt{P_i}$. Let us notice that the CFL coefficient can not be set to unity because we deal with unstructured two-dimensional meshes, thus it obeys the standard restriction $\mathrm{CFL} < 1/d$. These schemes are proven in [29, 21] to be stable and capable of describing different collisional regimes as well as consistent with the limit model of the compressible Euler equations in the case of single species kinetic equations. In the following part, we extend this analysis to the case of mixtures showing consistency with the different hydrodynamic limits (29) and (33).

3.4. On the preservation of the asymptotic states

We start by rewriting (78) and (80) by making explicit the contribution of the diagonally implicit BGK operators in the stage evaluation. We reduce then to the following form

$$\begin{aligned}
\bar{F}^{(l)}_{1,k,i} &= \bar{f}^{n}_{1,k,i} - \Delta t \sum_{m=1}^{l-1} \tilde{a}_{lm} \left(L^{W,(m)}_{1,k,i} - G^{W,(m)}_{1,k,i} \right) + \frac{\Delta t}{\varepsilon} \sum_{m=1}^{l-1} a_{lm} Q^{(m)}_{BGK_{1,1},k} + \frac{\Delta t \alpha}{\varepsilon} \sum_{m=1}^{l-1} a_{lm} Q^{(m)}_{BGK_{1,2},k} \\
&+ \frac{\Delta t}{\varepsilon} a_{mm} \nu_{11} (\bar{\mathcal{E}}^{(l)}_{11,k,i}[\bar{U}_1, \bar{U}_2] - \bar{F}^{(l)}_{1,i,k}) + \frac{\Delta t \alpha}{\varepsilon} a_{mm} \nu_{12} (\bar{\mathcal{E}}^{(l)}_{12,k,i}[\bar{U}_1, \bar{U}_2] - \bar{F}^{(l)}_{1,i,k}) \qquad (85) \\
\bar{F}^{(l)}_{2,k,i} &= \bar{f}^{n}_{2,k,i} - \Delta t \sum_{m=1}^{l-1} \tilde{a}_{lm} \left(L^{W,(m)}_{2,k,i} - G^{W,(m)}_{2,k,i} \right) + \frac{\Delta t}{\varepsilon} \sum_{m=1}^{l-1} a_{lm} Q^{(m)}_{BGK_{2,2},k} + \frac{\Delta t \alpha}{\varepsilon} \sum_{m=1}^{l-1} a_{lm} Q^{(m)}_{BGK_{2,1},k} \\
&+ \frac{\Delta t}{\varepsilon} a_{mm} \nu_{21} (\bar{\mathcal{E}}^{(l)}_{21,k,i}[\bar{U}_1, \bar{U}_2] - \bar{F}^{(l)}_{2,i,k}) + \frac{\Delta t \alpha}{\varepsilon} a_{mm} \nu_{22} (\bar{\mathcal{E}}^{(l)}_{22,k,i}[\bar{U}_1, \bar{U}_2] - \bar{F}^{(l)}_{2,i,k}). \qquad (86)
\end{aligned}$$

Moving on the left hand side the linear implicit term corresponding to the evaluation of the cell average stage level gives

$$\begin{aligned}
\bar{F}^{(l)}_{1,k,i} &= \frac{\varepsilon}{\varepsilon + a_{mm} \Delta t (\nu_{11} + \nu_{12} \alpha)} \left(\bar{f}^{n}_{1,k,i} - \Delta t \sum_{m=1}^{l-1} \tilde{a}_{lm} \left(L^{W,(m)}_{1,k,i} - G^{W,(m)}_{1,k,i} \right) \right) \\
&+ \frac{\Delta t}{\varepsilon + a_{mm} \Delta t (\nu_{11} + \nu_{12} \alpha)} \left(\sum_{m=1}^{l-1} a_{lm} Q^{(m)}_{BGK_{1,1},k} + \alpha \sum_{m=1}^{l-1} a_{lm} Q^{(m)}_{BGK_{1,2},k} \right) \\
&+ \frac{\Delta t a_{mm}}{\varepsilon + a_{mm} \Delta t (\nu_{11} + \nu_{12} \alpha)} \left(\nu_{11} (\bar{\mathcal{E}}^{(l)}_{11,k,i}[\bar{U}_1, \bar{U}_2]) + \alpha \nu_{12} (\bar{\mathcal{E}}^{(l)}_{12,k,i}[\bar{U}_1, \bar{U}_2]) \right) \qquad (87) \\
\bar{F}^{(l)}_{2,k,i} &= \frac{\varepsilon}{\varepsilon + a_{mm} \Delta t (\nu_{22} + \nu_{21} \alpha)} \left(\bar{f}^{n}_{2,k,i} - \Delta t \sum_{m=1}^{l-1} \tilde{a}_{lm} \left(L^{W,(m)}_{2,k,i} - G^{W,(m)}_{2,k,i} \right) \right) \\
&+ \frac{\varepsilon}{\varepsilon + a_{mm} (\nu_{22} + \nu_{21} \alpha)} \left(\sum_{m=1}^{l-1} a_{lm} Q^{(m)}_{BGK_{2,2},k} + \alpha \sum_{m=1}^{l-1} a_{lm} Q^{(m)}_{BGK_{2,1},k} \right) \\
&+ \frac{\Delta t a_{mm}}{\varepsilon + a_{mm} \Delta t (\nu_{22} + \nu_{21} \alpha)} \left(\nu_{11} (\bar{\mathcal{E}}^{(l)}_{22,k,i}[\bar{U}_1, \bar{U}_2]) + \alpha \nu_{12} (\bar{\mathcal{E}}^{(l)}_{21,k,i}[\bar{U}_1, \bar{U}_2]) \right). \qquad (88)
\end{aligned}$$

Now, we discuss separately the case $\alpha = O(1)$ from the case $\alpha = \varepsilon$. We start by considering the case $\alpha = 1$, i.e. the case in which the collisions among particles act at the same pace independently on the species to which they belong. In this situation, when $\varepsilon \to 0$, one gets from system (76) the compressible Euler equations (29) for a two components fluid. On the other hand, under the hypothesis of well-prepared initial data, i.e.

$$\bar{f}^{0}_{1,k,i} = \bar{\mathcal{E}}^{0}_{11,k,i}[\bar{U}_1, \bar{U}_2] = \bar{\mathcal{E}}^{0}_{12,k,i}[\bar{U}_1, \bar{U}_2], \quad \bar{f}^{0}_{2,k,i} = \bar{\mathcal{E}}^{0}_{22,k,i}[\bar{U}_1, \bar{U}_2] = \bar{\mathcal{E}}^{0}_{21,k,i}[\bar{U}_1, \bar{U}_2], \qquad (89)$$

for $i = 1, \dots, N_p,\ k = 1, \dots, N$, with $\mathbf{u}_1 = \mathbf{u}_2 = \mathbf{u}$ and $T_1 = T_2 = T$, one gets

$$\mathbf{u}_{12} = \mathbf{u}_{21} = \mathbf{u} \quad \text{and} \quad T_{12} = T_{21} = T\,, \qquad (90)$$

as already observed in (18). Thus, letting the scale parameter $\varepsilon \to 0$, gives for the stage values

$$\begin{aligned}
\bar{F}^{(l)}_{1,k,i} &= \frac{1}{\nu_{11} + \nu_{12}} \left(\nu_{11} (\bar{\mathcal{E}}^{(l)}_{11,k,i}[\bar{U}_1, \bar{U}_2]) + \nu_{12} (\bar{\mathcal{E}}^{(l)}_{12,k,i}[\bar{U}_1, \bar{U}_2]) \right) \\
\bar{F}^{(l)}_{2,k,i} &= \frac{1}{\nu_{21} + \nu_{22}} \left(\nu_{11} (\bar{\mathcal{E}}^{(l)}_{22,k,i}[\bar{U}_1, \bar{U}_2]) + \nu_{21} (\bar{\mathcal{E}}^{(l)}_{21,k,i}[\bar{U}_1, \bar{U}_2]) \right).
\end{aligned}$$

In fact, thanks to our choice of diagonally implicit tableaux in the IMEX schemes, the terms $Q^{(m)}_{BGK_{1,1},k}$, $Q^{(m)}_{BGK_{2,1},k}$, $Q^{(m)}_{BGK_{1,2},k}$ and $Q^{(m)}_{BGK_{2,2},k}$ are all identically equal to zero for $(m) < (l)$ being $\bar{f}^{n}_{1,k,i} = \mathcal{E}^{n}_{11,k,i}[\bar{U}_1, \bar{U}_2] = \mathcal{E}^{n}_{12,k,i}[\bar{U}_1, \bar{U}_2]$ and

$\bar{f}^n_{2,k,i} = \mathcal{E}^n_{22,k,i}[\bar{U}_1, \bar{U}_2] = \mathcal{E}^n_{21,k,i}[\bar{U}_1, \bar{U}_2]$ by hypothesis at time $t = 0$, i.e. $n = 0$, and then recursively at time n if true for $n = 1$. Moreover,under the same hypothesis, one has that $\nu_{11} = \nu_{12}$ and $\nu_{22} = \nu_{21}$, which means that each stage is projected over the corresponding equilibrium state at time level (l). Finally, being the IMEX schemes also stiffly accurate, i.e. since the last stage coincides with the numerical solution, we also obtain that

$$\begin{aligned} \bar{f}^{n+1}_{1,k,i} &= \frac{1}{2}\left((\bar{\mathcal{E}}^{n+1}_{11,k,i}[\bar{U}_1, \bar{U}_2]) + (\bar{\mathcal{E}}^{n+1}_{12,k,i}[\bar{U}_1, \bar{U}_2])\right) \\ \bar{f}^{n+1}_{2,k,i} &= \frac{1}{2}\left((\bar{\mathcal{E}}^{n+1}_{22,k,i}[\bar{U}_1, \bar{U}_2]) + (\bar{\mathcal{E}}^{n+1}_{21,k,i}[\bar{U}_1, \bar{U}_2])\right). \end{aligned}$$

It remains to discuss how the Maxwellian functions at time level (l) and at time $n + 1$ are obtained. To that aim, let us notice that $\mathcal{E}_{11,k,i}[\bar{U}_1, \bar{U}_2], \mathcal{E}_{12,k,i}[\bar{U}_1, \bar{U}_2], \mathcal{E}_{21,k,i}[\bar{U}_1, \bar{U}_2]$ and $\mathcal{E}_{22,k,i}[\bar{U}_1, \bar{U}_2]$ depend on mass, momentum and energy of the two species, i.e. on $\bar{U}_1$, $\bar{U}_2$. These latter can be explicitly computed by integrating in phase space the IMEX method (85) and (86). This gives

$$\bar{U}^{(l)}_{1,i} = \bar{U}^n_{1,i} - \Delta t \sum_{m=1}^{l} \tilde{a}_{lm} L^W_U(\bar{U}^{(m)}_{1,i}), \tag{91}$$

$$\bar{U}^{(l)}_{2,i} = \bar{U}^n_{2,i} - \Delta t \sum_{m=1}^{l} \tilde{a}_{lm} L^W_U(\bar{U}^{(m)}_{2,i}), \tag{92}$$

where $L^W_U(\bar{U}^{(m)}_{1,i})$ and $L^W_U(\bar{U}^{(m)}_{2,i})$ are high order evaluation of the macroscopic fluxes for the conserved quantities. These macroscopic fluxes are given by applying again the same CWENO reconstruction procedure to the macroscopic cell centered quantities $\bar{U}^n_{1,i}$ and $\bar{U}^n_{2,i}$. Moreover and most important, the contribution of the collision terms is zero at the macroscopic level. In fact, one has by definition of the Boltzmann and BGK operators that

$$\langle \phi_k, Q^{(m)}_{BGK_{1,1},k} \rangle = \langle \phi_k, Q^{(m)}_{BGK_{2,2},k} \rangle = \langle \phi_k, Q^{W,(m)}_{1,k} \rangle = \langle \phi_k, Q^{W,(m)}_{2,k} \rangle = 0.$$

On the other hand, thanks to the fact that $\mathbf{u}_1 = \mathbf{u}_2 = \mathbf{u}$ and $T_1 = T_2 = T$ at time $t = 0$, the quantities $\mathcal{E}^{(m)}_{12,k,i}[\bar{U}_1, \bar{U}_2]$ and $\mathcal{E}^{(m)}_{21,k,i}[\bar{U}_1, \bar{U}_2]$ share the same moments of $\bar{F}^{(m)}_{1,k,i}$ and $\bar{F}^{(m)}_{2,k,i}$ recursively from $m = 1$ because of the diagonally implicit tableau and therefore it also holds true that

$$\langle \phi_k, Q^{(m)}_{BGK_{1,2},k} \rangle = \langle \phi_k, Q^{(m)}_{BGK_{2,1},k} \rangle = 0.$$

As a consequence, Maxwellian distributions can be explicitly evaluated and then the scheme (85)-(86) is explicitly solvable. Finally, since the system (92) corresponds to a kinetic scheme for the compressible Euler equations (29), it follows that it remains true that $\mathbf{u}_1 = \mathbf{u}_2 = \mathbf{u}$ and $T_1 = T_2 = T$ for all times and so mixed Maxwellian functions coincide with single species ones. This is enough to prove that the schemes are asymptotic preserving and asymptotically accurate for the case $\alpha = 1$ under the hypothesis of well-prepared initial data.

We discuss now the case $\alpha = \varepsilon$. In this case, the intraspecies collisions are supposed to be much more frequent with respect to the collisions with the second species. This setting gives rise to the resonant collisions limit (33) discussed in Section 2.3.2. We suppose once again well-prepared initial data (with respect to the resonant collision case), hence setting

$$\bar{f}^0_{1,k,i} = \bar{\mathcal{E}}^0_{11,k,i}[\bar{U}_1, \bar{U}_2], \quad \bar{f}^0_{2,k,i} = \bar{\mathcal{E}}^0_{22,k,i}[\bar{U}_1, \bar{U}_2], \quad i = 1, \dots, N_p,\ k = 1, \dots, N, \tag{93}$$

with in general $\mathbf{u}_1 \neq \mathbf{u}_2$ and $T_1 \neq T_2$. This implies that $\bar{\mathcal{E}}^0_{21,k,i}[\bar{U}_1, \bar{U}_2] \neq \bar{\mathcal{E}}^0_{11,k,i}[\bar{U}_1, \bar{U}_2]$ and $\bar{\mathcal{E}}^0_{12,k,i}[\bar{U}_1, \bar{U}_2] \neq \bar{\mathcal{E}}^0_{22,k,i}[\bar{U}_1, \bar{U}_2]$. Under this setting, in the limit $\varepsilon \to 0$, we get from (87)-(88)

$$\bar{F}^{(l)}_{1,k,i} = \bar{\mathcal{E}}^{(l)}_{11,k,i}[\bar{U}_1, \bar{U}_2], \quad \bar{F}^{(l)}_{2,k,i} = \bar{\mathcal{E}}^{(l)}_{22,k,i}[\bar{U}_1, \bar{U}_2].$$

By replacing these values into equations (85)-(86) and by integrating in velocity space one then gets a finite volume

with CWENO reconstruction IMEX-Runge-Kutta scheme for the system (33). This reads

$$\bar{U}^{(l)}_{1,i} = \bar{U}^{n}_{1,i} - \Delta t \sum_{m=1}^{l} \tilde{a}_{lm} L^{W}_{U}(\bar{U}^{(m)}_{1,i}) + \Delta t \sum_{m=1}^{l} a_{lm} \langle \phi_k, Q^{(m)}_{BGK_{1,2},k} \rangle, \tag{94}$$

$$\bar{U}^{(l)}_{2,i} = \bar{U}^{n}_{2,i} - \Delta t \sum_{m=1}^{l} \tilde{a}_{lm} L^{W}_{U}(\bar{U}^{(b)}_{2,i}) + \Delta t \sum_{m=1}^{l} a_{lm} \langle \phi_k, Q^{(m)}_{BGK_{2,1},k} \rangle, \tag{95}$$

where the terms $\langle \phi_k, Q^{(m)}_{BGK_{1,2},k} \rangle$ and $\langle \phi_k, Q^{(m)}_{BGK_{2,1},k} \rangle$ correspond to the integration in velocity space of the mixed BGK operators against the collision invariants ϕ_k. These terms are, contrarily to the case of $\alpha = 1$, different from zero since the moments of the mixed Maxwellians do not coincide with the moments of the distribution function in general. Let us notice that, in this case, the macroscopic set of equations discretizing the resonant collision dynamics is diagonally implicit in the source terms $\langle \phi_k, Q^{(m)}_{BGK_{1,2},k} \rangle$ and $\langle \phi_k, Q^{(m)}_{BGK_{2,1},k} \rangle$ while in the case $\alpha = 1$ the macroscopic dynamic was fully explicit. These implicit terms are responsible for the right hand side terms appearing in (33). For the first species, they read

$$-\mu\, n_1\, n_2\, \frac{m}{1+m}\, (\mathbf{u}_1 - \mathbf{u}_2), \tag{96}$$

for the moment equations and

$$-\mu\, n_1\, n_2\, \frac{m}{(1+m)^2} \Big[(\mathbf{u}_1 + m\, \mathbf{u}_2) \cdot (\mathbf{u}_1 - \mathbf{u}_2) + d\, (T_1 - T_2) \Big], \tag{97}$$

for the energy one, with opposite signs for the second species. However, since the density equations are fully explicit, these terms become simply linear with respect to the moments $\bar{U}^{(l)}_{1,i}$ and $\bar{U}^{(l)}_{2,i}$. Thus, in order to solve system (94)-(95) it is sufficient to invert a rank-two linear system for the coupled velocity field and successively a rank-two linear system for the coupled energy field once the velocity field is determined. This permits to compute the moments at the next time step and to define the new Maxwellian states $\bar{\mathcal{E}}^{n+1}_{11,k,i}[\bar{U}_1, \bar{U}_2]$ and $\bar{\mathcal{E}}^{n+1}_{22,k,i}[\bar{U}_1, \bar{U}_2]$, and eventually to advance in the computation. To conclude, let us observe that the scheme (94)-(95) represents a high order accurate method for the resonant collision model and, as such, asymptotic preservation and accuracy is proved also in this case.

4. Numerical results

In this section, the numerical validation of the finite volume IMEX Runge-Kutta scheme is assessed against a set of test problems. The numerical scheme is labeled with FVRK-M and it is applied to the novel mixed Boltzmann–BGK model with second order of accuracy in space and time (the ARS(2,2,2) IMEX scheme [3] is adopted). Dominant and resonant collision regimes refer to the limit models presented in Section 2.3.1 and 2.3.2, respectively. Numerical convergence studies on smooth fluid flows with variable Knudsen numbers are carried out first, then shock capturing properties are proven to be achieved by the numerical method through Riemann problems in 1D and 2D. Finally, a more complex test case involving the interaction of two bubbles embedded into a background gas is set up and discussed.

The velocity space is discretized by means of a Cartesian mesh, thus the mesh spacing is given by $\Delta v_{x_1} = \Delta v_{x_2} := \Delta v$. A total number of $N = 32 \times 32 = 1024$ equal elements is used, unless otherwise stated. This also corresponds to the number of modes N_M adopted in the spectral method for the solution of the Boltzmann collision operator.

The initial data are given in terms of the macroscopic variables $U_i = (\rho, u_x, u_y, T)_i$ for gas 1 and 2, hence assigning U_1 and U_2, respectively. The distribution function is initially prescribed as a Maxwellian with the moments corresponding to U_i.

4.1. Numerical convergence studies at different Knudsen numbers

The numerical convergence of the FVRK-M schemes is studied relying on the smooth isentropic vortex test case introduced in [44] for the Euler equations of compressible gas dynamics. The aim of this test is to numerically investigate the rate of convergence of the novel methods, thus we simply consider the same initial condition for both species in the mixture. Let $\Omega = [0; 10] \times [0; 10]$ be the computational domain, where periodic boundaries are

set everywhere. A sequence of refined unstructured triangular meshes is used to discretize the physical space, with characteristic mesh size $h(\Omega) = (\sum_{i=1}^{N_P} h_i)/N_P$ with $h_i = \sqrt{|P_i|}$ and $|P_i|$ denoting the surface of the cell P_i. The velocity space has bounds within $\mathcal{V} = [-10; 10]^2$ and the initial condition is given by $U_1 = U_2 = U$ with

$$U = (\rho, u_x, u_y, T) = (1 + \delta\rho, \delta u_x, \delta u_y, \delta T), \tag{98}$$

where the space–dependent perturbations for temperature δT, density $\delta\rho$ and velocity $(\delta u_x, \delta u_y)$ are

$$\delta T = -\frac{(\gamma-1)\beta^2}{8\gamma\pi^2} e^{1-r^2}, \quad \delta\rho = (1+\delta T)^{\frac{1}{\gamma-1}} - 1, \quad \begin{pmatrix} \delta u_x \\ \delta u_y \end{pmatrix} = \frac{\beta}{2\pi} e^{\frac{1-r^2}{2}} \begin{pmatrix} -(y-5) \\ (x-5) \end{pmatrix}, \tag{99}$$

with $\beta = 5$ and $r = \sqrt{x^2 + y^2}$ denoting the generic radial coordinate. The ratio of specific heats for each gas of the mixture is set to $\gamma = 2$. A unity mass ratio is assumed. The final time of the simulation is chosen to be $t_f = 0.1$ and the errors are computed in L_1 norm as

$$L_1 = \int_\Omega \left| U_{ref}(x, y) - U^W(x, y) \right| dx\, dy, \tag{100}$$

where $U^W(x, y)$ is the second order Finite Volume solution for the macroscopic quantities, while $U_{ref}(x, y)$ is a given *reference solution*. The initial condition corresponds to the analytical solution for this smooth stationary vortex flow *only* in the hydrodynamics limit, i.e. $\varepsilon \to 0$. Since no analytical solution is available for arbitrary values of the Knudsen number, the reference solution $U_{ref}(x, y)$, needed for computing the error norms, is obtained by running the test case on a very fine physical mesh while keeping the same discretization in the velocity space. Mesh refinement is carried out for triangular meshes relying on conforming finite element discretizations, hence each element is split into sub-elements with the isotropic refinement factor χ. Specifically, a total number of sub-elements $N_R = \chi^2$ is generated, as depicted in Figure 2. The reference triangular mesh is constructed by applying a refinement factor of $\chi = 8$ to the coarsest grid used for the convergence analysis which counts $N_P = 10^2$ elements, thus subdividing each triangle into $N_R = 64$ sub-triangles. Then, the numerical solution on each coarse grid is interpolated on the reference mesh and the errors can be computed.

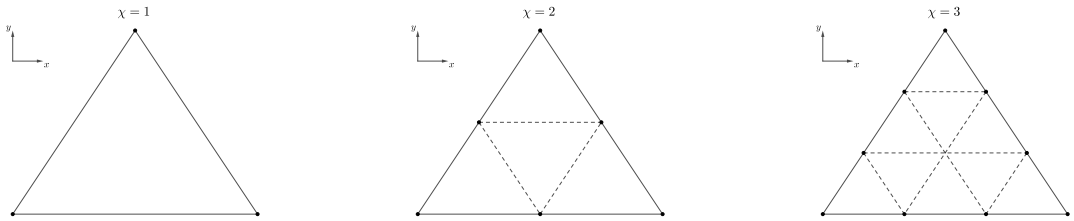

Figure 2: Convergence analysis. Example of isotropic mesh refinement used for convergence analysis with triangular meshes and refinement factor $\chi = 1$ ($N_R = 1$), $\chi = 2$ ($N_R = 4$) and $\chi = 3$ ($N_R = 9$).

Tables 2 and 3 report the error norms and convergence rates for the dominant and resonant collision regimes, respectively. Three different Knudsen numbers are considered, namely $\varepsilon = 10^{-6}$, $\varepsilon = 10^{-4}$ and $\varepsilon = 10^{-2}$, and the norms refer to number densities n_1 and n_2 as well as temperatures T_1 and T_2. In all cases we observe that the formal second order of accuracy in space and time is achieved, demonstrating that the space-time accuracy of the FVRK-M schemes is independent of the stiffness of the problem under consideration, both in terms of ε and α.

4.2. Shock tube problems

In order to check the capability of the scheme to capture flow discontinuities, a one–dimensional Riemann problem is solved with different fluid conditions. Indeed, the shock tube test is run using three values of the Knudsen number,

Table 2: Numerical convergence results for the mixed Boltzmann–BGK model using second order FVRK-M schemes at time $t_f = 0.1$ with $\varepsilon = [10^{-6}, 10^{-4}, 10^{-2}]$ and $\alpha = 1$ on a sequence of refined triangular meshes of size $h(\Omega)$ obtained with refinement factor $\chi = [2, 3, 4, 5]$. The errors are measured in L_1 norm and refer to the variables n_1 (number density of gas 1), T_1 (temperature of gas 1), n_2 (number density of gas 2), T_2 (temperature of gas 2). *Dominant collision* regime.

$\varepsilon = 10^{-6}, \alpha = 1$

$h(\Omega)$	n_{1L_1}	$O(n_1)$	T_{1L_1}	$O(T_1)$	n_{2L_1}	$O(n_2)$	T_{2L_1}	$O(T_2)$
2.87E-01	6.369E-02	-	1.551E-01	-	1.038E-01	-	2.487E-01	-
1.91E-01	2.959E-02	1.89	6.964E-02	1.97	4.757E-02	1.92	1.101E-01	2.01
1.44E-01	1.584E-02	2.17	3.619E-02	2.27	2.510E-02	2.22	5.691E-02	2.29
1.15E-01	1.052E-02	1.83	2.410E-02	1.82	1.636E-02	1.92	3.740E-02	1.88

$\varepsilon = 10^{-4}, \alpha = 1$

$h(\Omega)$	n_{1L_1}	$O(n_1)$	T_{1L_1}	$O(T_1)$	n_{2L_1}	$O(n_2)$	T_{2L_1}	$O(T_2)$
2.87E-01	6.370E-02	-	1.551E-01	-	1.037E-01	-	2.486E-01	-
1.91E-01	2.959E-02	1.89	6.964E-02	1.97	4.754E-02	1.92	1.101E-01	2.01
1.44E-01	1.584E-02	2.17	3.619E-02	2.28	2.508E-02	2.22	5.689E-02	2.29
1.15E-01	1.052E-02	1.83	2.410E-02	1.82	1.635E-02	1.92	3.738E-02	1.88

$\varepsilon = 10^{-2}, \alpha = 1$

$h(\Omega)$	n_{1L_1}	$O(n_1)$	T_{1L_1}	$O(T_1)$	n_{2L_1}	$O(n_2)$	T_{2L_1}	$O(T_2)$
2.87E-01	6.380E-02	-	1.553E-01	-	1.013E-01	-	2.435E-01	-
1.91E-01	2.947E-02	1.90	6.959E-02	1.98	4.610E-02	1.94	1.073E-01	2.02
1.44E-01	1.566E-02	2.20	3.612E-02	2.28	2.408E-02	2.26	5.516E-02	2.31
1.15E-01	1.033E-02	1.86	2.405E-02	1.82	1.573E-02	1.91	3.639E-02	1.86

Table 3: Numerical convergence results for the mixed Boltzmann–BGK model using second order FVRK-M schemes at time $t_f = 0.1$ with $\varepsilon = [10^{-6}, 10^{-4}, 10^{-2}]$ and $\alpha = [10^{-6}, 10^{-4}, 10^{-2}]$ on a sequence of refined triangular meshes of size $h(\Omega)$ obtained with refinement factor $\chi = [2, 3, 4, 5]$. The errors are measured in L_1 norm and refer to the variables n_1 (number density of gas 1), T_1 (temperature of gas 1), n_2 (number density of gas 2), T_2 (temperature of gas 2). *Resonant collision* regime.

$\varepsilon = 10^{-6}, \alpha = 10^{-6}$

$h(\Omega)$	n_{1L_1}	$O(n_1)$	T_{1L_1}	$O(T_1)$	n_{2L_1}	$O(n_2)$	T_{2L_1}	$O(T_2)$
2.87E-01	6.431E-02	-	1.570E-01	-	1.016E-01	-	2.449E-01	-
1.91E-01	2.987E-02	1.89	7.050E-02	1.97	4.653E-02	1.93	1.083E-01	2.01
1.44E-01	1.598E-02	2.17	3.673E-02	2.27	2.448E-02	2.23	5.590E-02	2.30
1.15E-01	1.056E-02	1.86	2.439E-02	1.83	1.609E-02	1.88	3.685E-02	1.87

$\varepsilon = 10^{-4}, \alpha = 10^{-4}$

$h(\Omega)$	n_{1L_1}	$O(n_1)$	T_{1L_1}	$O(T_1)$	n_{2L_1}	$O(n_2)$	T_{2L_1}	$O(T_2)$
2.87E-01	6.429E-02	-	1.569E-01	-	1.016E-01	-	2.447E-01	-
1.91E-01	2.985E-02	1.89	7.048E-02	1.97	4.650E-02	1.93	1.082E-01	2.01
1.44E-01	1.596E-02	2.18	3.671E-02	2.27	2.445E-02	2.23	5.581E-02	2.30
1.15E-01	1.054E-02	1.86	2.438E-02	1.83	1.607E-02	1.88	3.679E-02	1.87

$\varepsilon = 10^{-2}, \alpha = 10^{-2}$

$h(\Omega)$	n_{1L_1}	$O(n_1)$	T_{1L_1}	$O(T_1)$	n_{2L_1}	$O(n_2)$	T_{2L_1}	$O(T_2)$
2.87E-01	6.354E-02	-	1.550E-01	-	1.000E-01	-	2.390E-01	-
1.91E-01	2.919E-02	1.92	6.926E-02	1.99	4.521E-02	1.96	1.049E-01	2.03
1.44E-01	1.542E-02	2.22	3.589E-02	2.29	2.346E-02	2.28	5.373E-02	2.32
1.15E-01	1.016E-02	1.87	2.390E-02	1.82	1.536E-02	1.90	3.558E-02	1.85

namely $\varepsilon = 10^{-6}$, $\varepsilon = 10^{-4}$ and $\varepsilon = 10^{-2}$, and both dominant and resonant collision regimes are investigated in the gas mixture dynamics. The computational domain is the box $\Omega = [-0.5; 0.5] \times [-0.05; 0.05]$ discretized with $N_P = [100 \times 10]$ polygonal control volumes with characteristic mesh size of $h(\Omega) = 0.01$. Slip wall boundary conditions are set in $y-$direction, while Dirichlet boundaries are imposed in the $x-$direction. The final time is chosen to be $t_f = 0.05$, so that no waves exit the physical domain. The velocity space is defined within the interval $\mathcal{V} = [-15; 15]^2$ and the initial condition is given by a left $\mathbf{Q}_L = (U_1, U_2)_L$ and a right $\mathbf{Q}_R = (U_1, U_2)_R$ state separated by a discontinuity located at $x = 0$:

$$\begin{cases} \mathbf{Q}_L &= (1, 0, 0, 5, 1, 0, 0, 5), \\ \mathbf{Q}_R &= (0.125, 0, 0, 0.5, 0.125, 0, 0, 4). \end{cases} \tag{101}$$

The mass ratio between the gases is $m_2/m_1 = 0.6$. Since the computational domain is discretized by means of a two–dimensional unstructured mesh, although solving a one–dimensional problem, this test can also demonstrate the ability of maintaining a one–dimensional structure of the numerical solution even if the element edges are not aligned with the fluid motion.

Figure 3 shows the results obtained in the fluid limit $\varepsilon = 10^{-6}$ for the resonant collision regime with $\alpha = 10^{-6}$. A comparison against the exact solution of the Euler equations of compressible gas dynamics is proposed for gas 1, highlighting the correct behavior of our scheme. Furthermore, a three-dimensional view of the number density profile n_1 is depicted, proving that the two–dimensional polygonal mesh does not affect the symmetry of the solution along the $y-$axis.

Figure 4 is concerned with the dominant collision regime for different values of the Knudsen number, thus we fix $\alpha = 1$. The temperature of both gases collapses to the same profile, as expected from the limit analysis of the continuous model in the case of dominant collisions. When dealing with $\varepsilon = 10^{-2}$, the highly rarefied gases have still to reach the dominant collision regime, thus they exhibit different temperatures at the final time of the simulation.

The same set of simulations has also been carried out in the resonant collision regime, thus imposing $\alpha = \varepsilon$ for $\varepsilon = [10^{-6}, 10^{-4}, 10^{-2}]$. Here, the interaction between the gases almost disappears and each single gas is not mixed with the other one. Therefore, one can solve the Boltzmann model for one single species and compare the solution against the results obtained from the mixture Boltzmann–BGK model. Indeed, this is shown in Figure 5 for gas 1, where a perfect overlapping with the Boltzmann solution can be appreciated. This demonstrates the consistency of the mixed Boltzmann–BGK model which retrieves the Boltzmann model for one gas in the case of resonant collisions.

4.3. Two–dimensional Riemann problem

The next test handles more complex wave patterns which arise from a genuinely two-dimensional Riemann problem. The initial condition is taken from [32] and modified in order to fit the Boltzmann–BGK model for gas mixture. The computational domain is $\Omega = [-0.5; 0.5] \times [-0.5; 0.5]$ and slip wall boundaries are assigned everywhere. A polygonal grid composed of $N_P = 150^2$ control volumes is used to pave the domain, thus involving a total number of approximately $69 \cdot 10^6$ degrees of freedom. We use a velocity space spanning the domain $\mathcal{V} = [-15; 15]^2$. The initial condition is given by four piecewise constant states defined in each quadrant of the two–dimensional coordinate system:

$$U_{1,2}(\mathbf{x}, 0) = \begin{cases} U_I &= (2, 0, 0, 1, 1.5, 0, 0, 4/3) \quad \text{if} \quad x > 0 \wedge y > 0, \\ U_{II} &= (1, 0, 0, 1, 0.5, 0, 0, 2) \quad \text{if} \quad x \leq 0 \wedge y > 0, \\ U_{III} &= (2, 0, 0, 1, 1.5, 0, 0, 4/3) \quad \text{if} \quad x \leq 0 \wedge y \leq 0, \\ U_{IV} &= (1, 0, 0, 1, 0.5, 0, 0, 2) \quad \text{if} \quad x > 0 \wedge y \leq 0. \end{cases} \tag{102}$$

The Knudsen number is $\varepsilon = 10^{-5}$, thus the hydrodynamic limit is approached and shocks are more evident. In this way the numerical scheme is tested against more stringent flow conditions rather than in rarefied gas regimes. The interaction between the gases is controlled by imposing $\alpha = 0.8$, hence allowing almost full mixture between the species. Figure 6 depicts the distribution of the number density and temperature for both gases with mass ratio $m_2/m_1 = 0.5$, while in Figure 7 the same plots are proposed for the case $m_2/m_1 = 2$. Several shocks are generated which interact simultaneously at the center of the domain as well as along the boundaries. The numerical scheme is capable of maintaining stability because of the nonlinear CWENO spatial reconstruction and the IMEX time discretization. Due to the gas interaction, temperature tends to converge to the same profile in both cases. The lower is the mass ratio, the stronger are the shocks generated in gas 2, as evident comparing the results in the bottom left panel

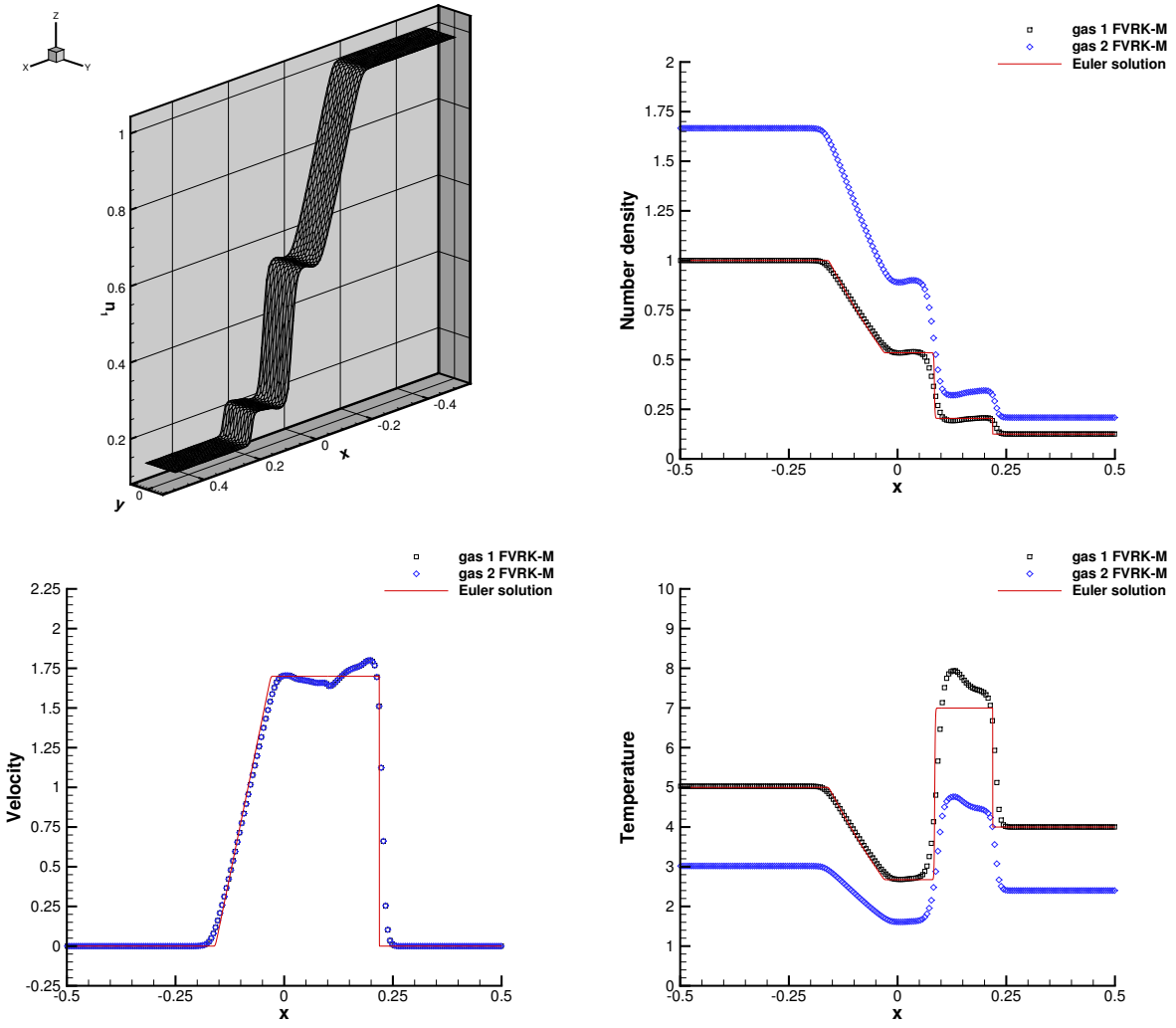

Figure 3: Shock tube problem at time $t_f = 0.05$ with second order FV IMEX-RK scheme for mixed Boltzmann–BGK model. Resonant collision regime with $[\varepsilon, \alpha] = [10^{-6}, 10^{-6}]$. 1D cut along the x-axis through the numerical results for number density (top right), horizontal velocity (bottom left) and temperature (bottom right). The solution of the Euler equations is shown in red solid line for comparison purposes. A three-dimensional view of the number density profile for gas 1 is plot in the top left panel.

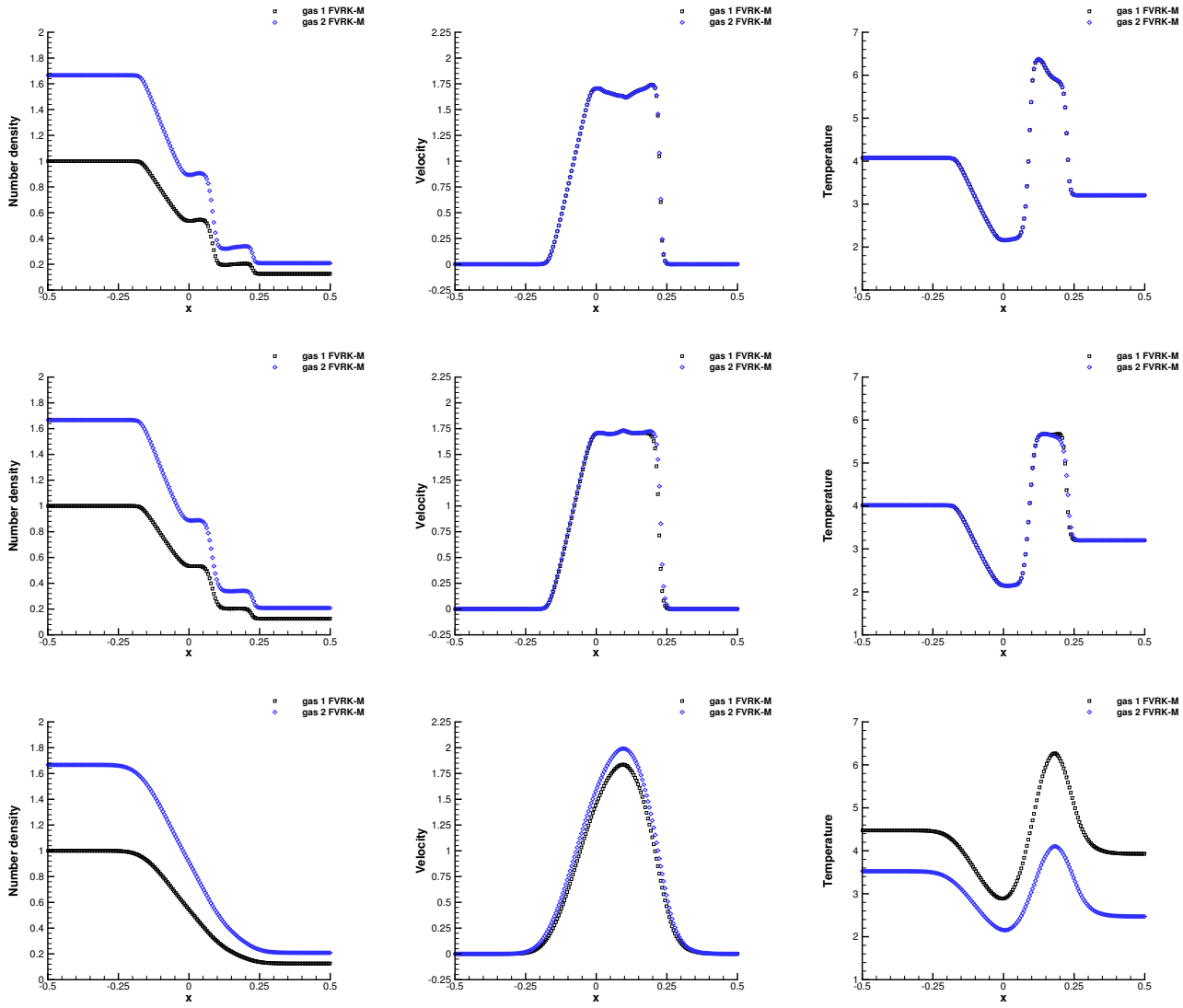

Figure 4: Shock tube problem at time $t_f = 0.05$ with second order FV IMEX-RK scheme for mixed Boltzmann–BGK model. Dominant collision regime with $[\varepsilon, \alpha] = [10^{-6}, 1]$ (top row), $[\varepsilon, \alpha] = [10^{-4}, 1]$ (middle row), $[\varepsilon, \alpha] = [10^{-4}, 1]$ (bottom row). 1D cut along the x-axis through the numerical results for number density (left), horizontal velocity (middle) and temperature (right).

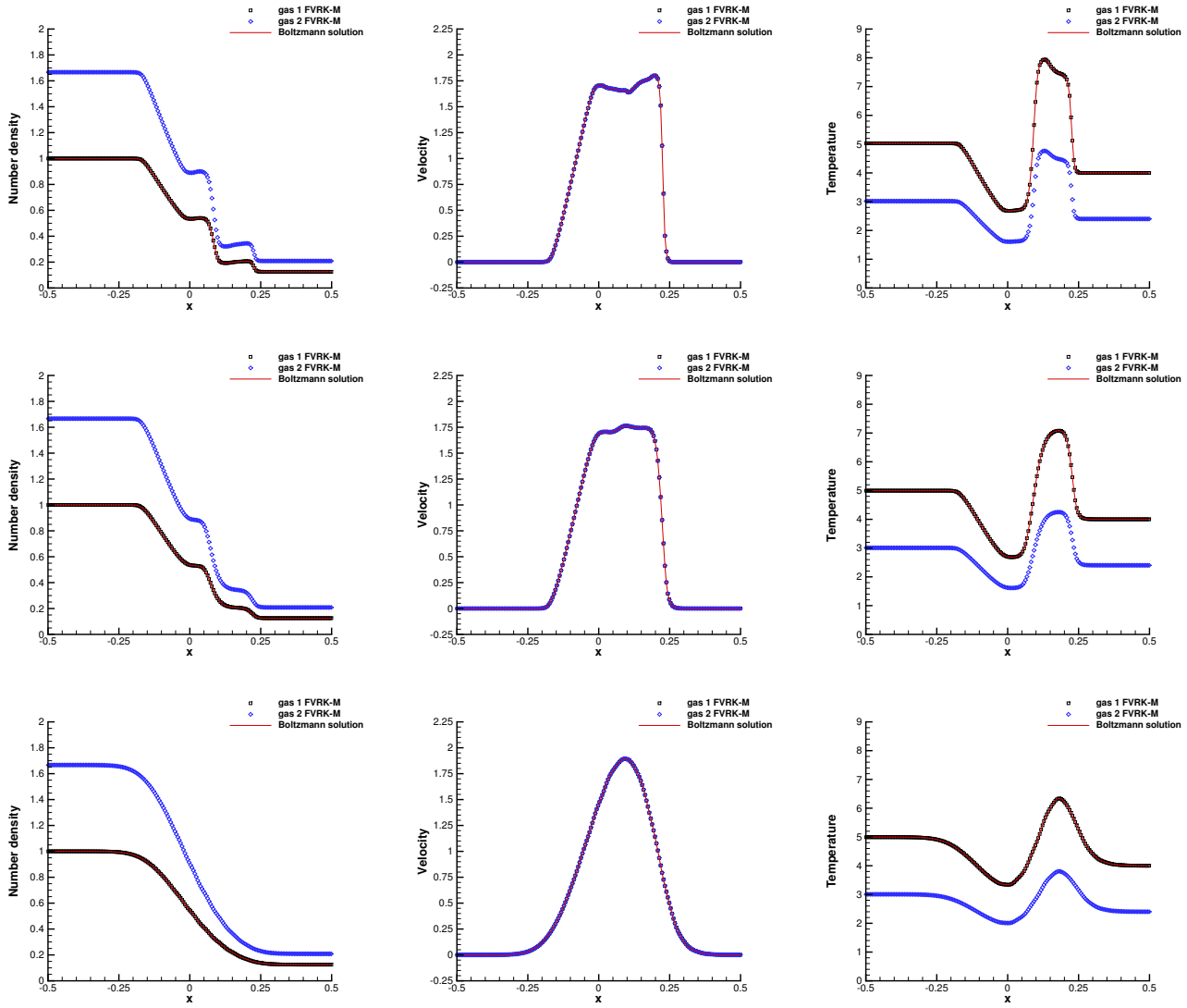

Figure 5: Shock tube problem at time $t_f = 0.05$ with second order FV IMEX-RK scheme for mixed Boltzmann–BGK model. Resonant collision regime with $[\varepsilon, \alpha] = [10^{-6}, 10^{-6}]$ (top row), $[\varepsilon, \alpha] = [10^{-4}, 10^{-4}]$ (middle row), $[\varepsilon, \alpha] = [10^{-2}, 10^{-2}]$ (bottom row). 1D cut along the x-axis through the numerical results for number density (left), horizontal velocity (middle) and temperature (right). The solution of the Boltzmann model is computed according to [19] and it is shown in red solid line for comparison purposes against gas 1.

of Figures 6-7. This test proves that the numerical scheme can deal with shocks and strong discontinuities that exhibit a truly multidimensional behavior. Furthermore, the results are independent of the Knudsen number and the type of collision among the species, governed by the parameter α. Different mass ratio between the gases can also be easily handled by the FVRK-M scheme.

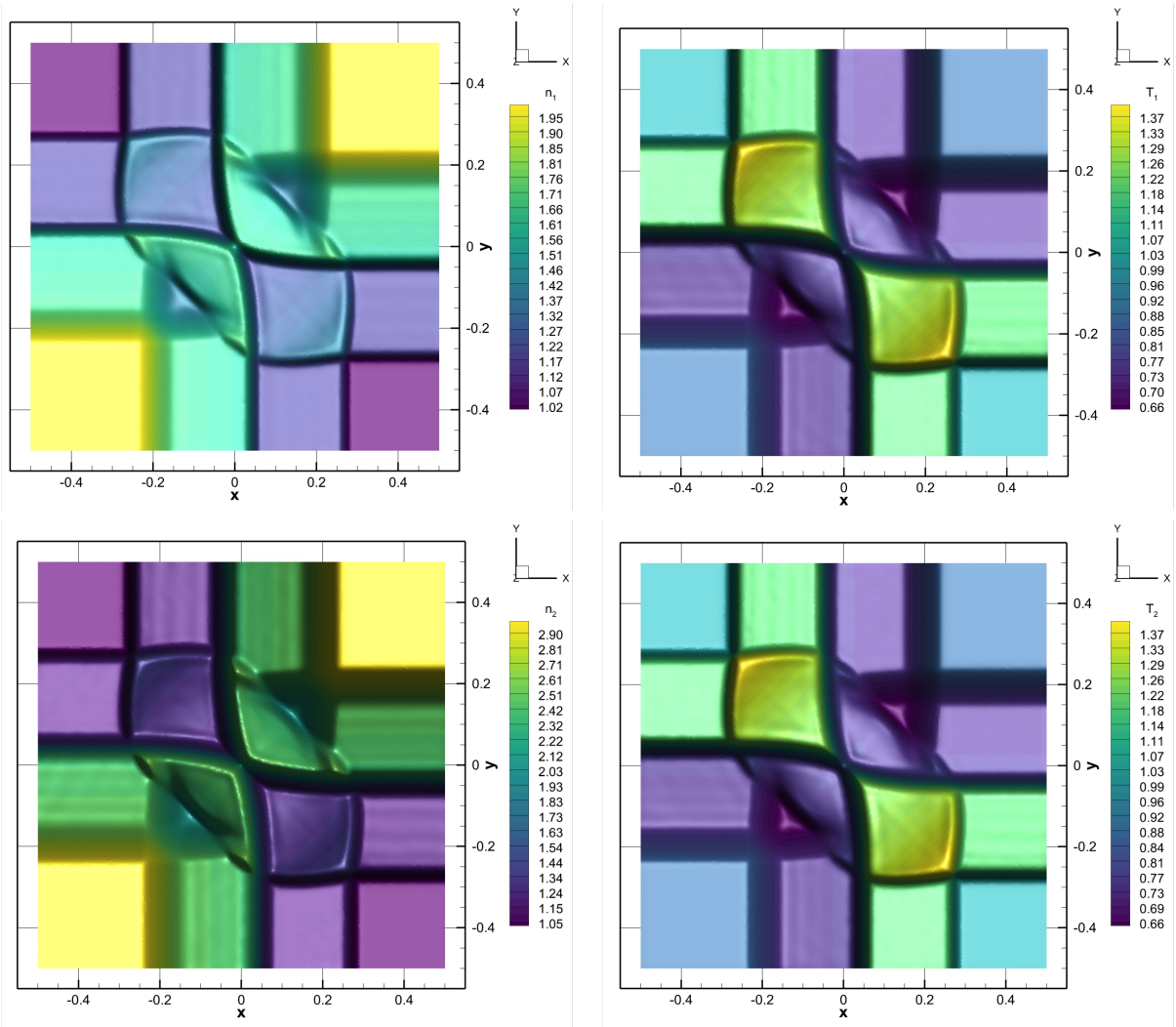

Figure 6: Two-dimensional Riemann problem at time $t_f = 0.15$ with second order FV IMEX-RK scheme for mixed Boltzmann–BGK model. Dominant collision regime with $[\varepsilon, \alpha] = [10^{-5}, 0.8]$ and mass ratio $m_2/m_1 = 0.5$. Distribution of number density n_1 (top left), temperature T_1 (top right), number density n_2 (bottom left), temperature T_2 (bottom right). 40 contour levels within the maximum and minimum value of each variable are used.

4.4. Interaction of two bubbles of gas

As last test case, we propose to simulate the interaction of two colliding bubbles of gas embedded into another gas which is at rest. The computational domain is given by $\Omega = [-0.5; 0.5] \times [-0.5; 0.5]$ and slip wall boundaries are set everywhere. The physical space is discretized using a total number of $N_P = 100^2$ polygonal cells, while the velocity space is bounded in the interval $\mathcal{V} = [-12; 12]^2$, thus the problem size counts a total number of approximately $30 \cdot 10^6$ degrees of freedom. The initial condition for gas 1 is simply given as a background state and reads $U_1 = (1, 0, 0, 1)$.

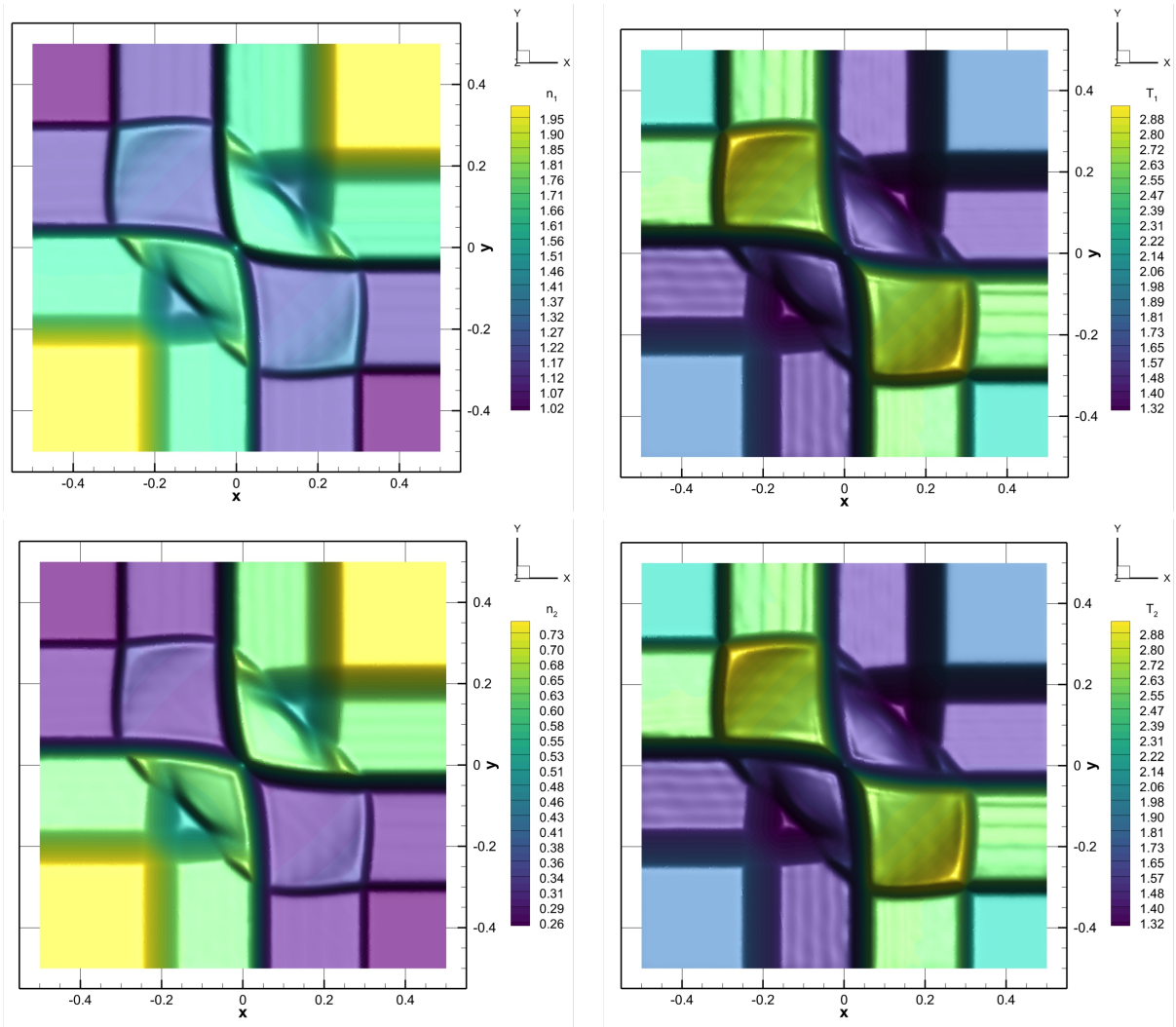

Figure 7: Two-dimensional Riemann problem at time $t_f = 0.15$ with second order FV IMEX-RK scheme for mixed Boltzmann–BGK model. Dominant collision regime with $[\varepsilon, \alpha] = [10^{-5}, 0.8]$ and mass ratio $m_2/m_1 = 2$. Distribution of number density n_1 (top left), temperature T_1 (top right), number density n_2 (bottom left), temperature T_2 (bottom right). 40 contour levels within the maximum and minimum value of each variable are used.

The second species with state U_2 is initially distributed as follows:

$$U_2(\mathbf{x},0) = \begin{cases} (2,2,0,1) & \text{if } r_1 < R_b, \\ (2,-2,0,1) & \text{if } r_2 < R_b, \\ (0.1,0,0,1) & \text{otherwise,} \end{cases} \tag{103}$$

with the radial positions $r_1 = \sqrt{(x-X_1)^2+(y-Y_1)^2}$ and $r_2 = \sqrt{(x-X_2)^2+(y-Y_2)^2}$. The first bubble is centered at $(X_1, Y_1) = (-0.5, 0)$, while the second bubble is centered at $(X_2, Y_2) = (0.5, 0)$, and they are both assigned a size of radius $R_b = 0.2$. Figure 8 shows the initial condition for number density n_2 and horizontal velocity u_2 as well as the unstructured polygonal mesh used for carrying out the computation.

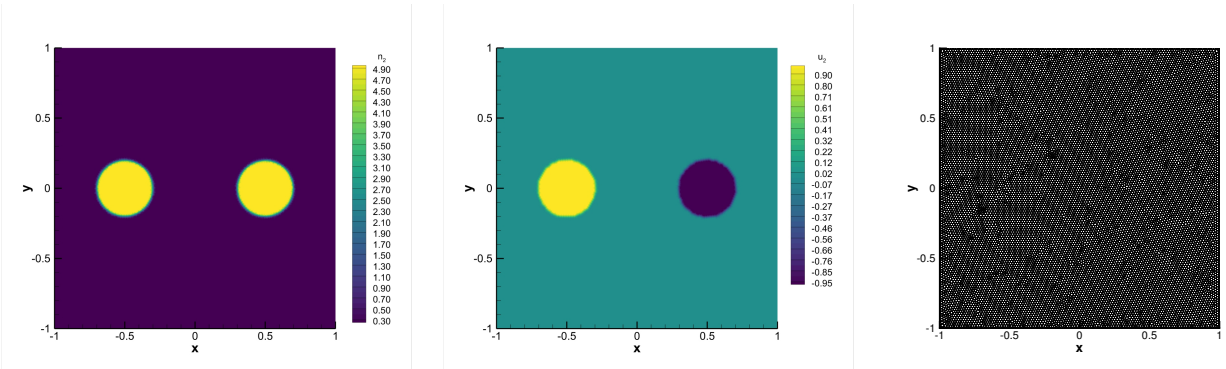

Figure 8: Interaction of two bubbles at initial time $t = 0$. Distribution of number density n_2 (left) and horizontal velocity u_2 (right) of gas 2 and polygonal computational mesh (right).

A relatively long time simulation is considered, by setting the final time to $t_f = 0.8$, hence allowing shock and contact waves to travel several times across the domain and being reflected by the boundary walls as well as by interactions among themselves. The Knudsen number is fixed at the value $\varepsilon = 10^{-4}$ and the mass ratio is chosen to be $m_2/m_1 = 0.4$. Figures 9 and 10 collect the time evolution of number density n_1 and temperature T_1, respectively, in the dominant collision regime with $\alpha = 0.8$. One can notice that the numerical solution exhibits an excellent preservation of symmetry, despite the fully unstructured mesh and the complex structure of the flow. The same wave patterns generated by the number density are also qualitatively recovered by the corresponding temperature distribution. Boundary conditions reflect the impinging waves by emitting them back into the computational domain, hence giving rise to additional interactions inside the physical space. At the final time the solution looks quite complicated with several shocks that are still symmetrically distributed over the domain.

Finally, the same simulation is run approaching the resonant collision regime, hence setting $\alpha = 10^{-3}$. Figures 11 and 12 deal with a comparison against the dominant collision simulation for both number density n_2 and temperature T_2, respectively, at output times $t = 0.2$, $t = 0.5$ and $t = 0.8$. The comparison shows that in the resonant collision regime the mixing process is inhibited, thus gas 2 follows its own dynamics that is responsible for a stronger intersection of the two bubbles, which change and deform their initial shape much faster than in the dominant collision regime, as can be noticed in Figure 11 for n_2. The same behavior is also evident in the temperature distribution T_2 in Figure 12, where the mixture occurring for $\alpha = 0.8$ mitigates the impact between the two bubbles by letting gas 2 interacting and spreading within gas 1. Let us also observe that the order of magnitude of both n_2 and T_2 undergoes a remarkable change when passing from dominant to resonant collision regime.

5. Conclusions

In this work, we have presented a new model that aims at describing the dynamics of a binary mixture of inert gases. This models relies on the original Boltzmann equation for governing collisions among particles of the same species, while it makes use of simpler and computationally efficient BGK relaxation terms to consider the interspecies

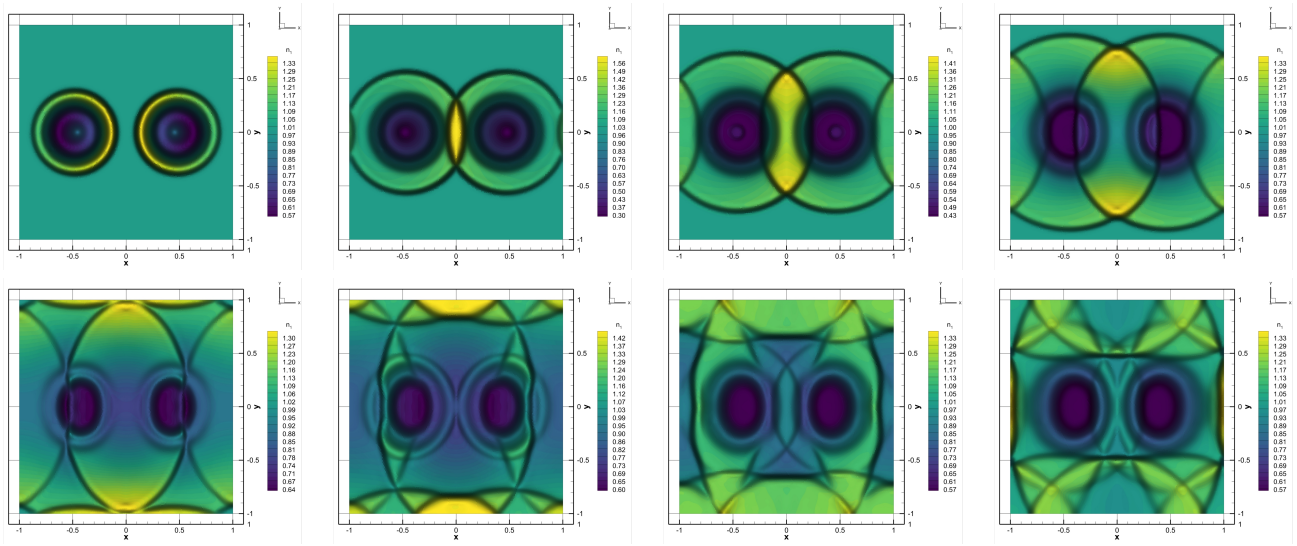

Figure 9: Interaction of two bubbles with $[\varepsilon, \alpha] = [10^{-4}, 0.8]$. Distribution of number density n_1 at times $t = [0.1, 0.2, 0.3, 0.4, 0.5, 0.6, 0.7, 0.8]$ (from top left to bottom right). 40 contour levels within the maximum and minimum value of n_1 at each output time are used.

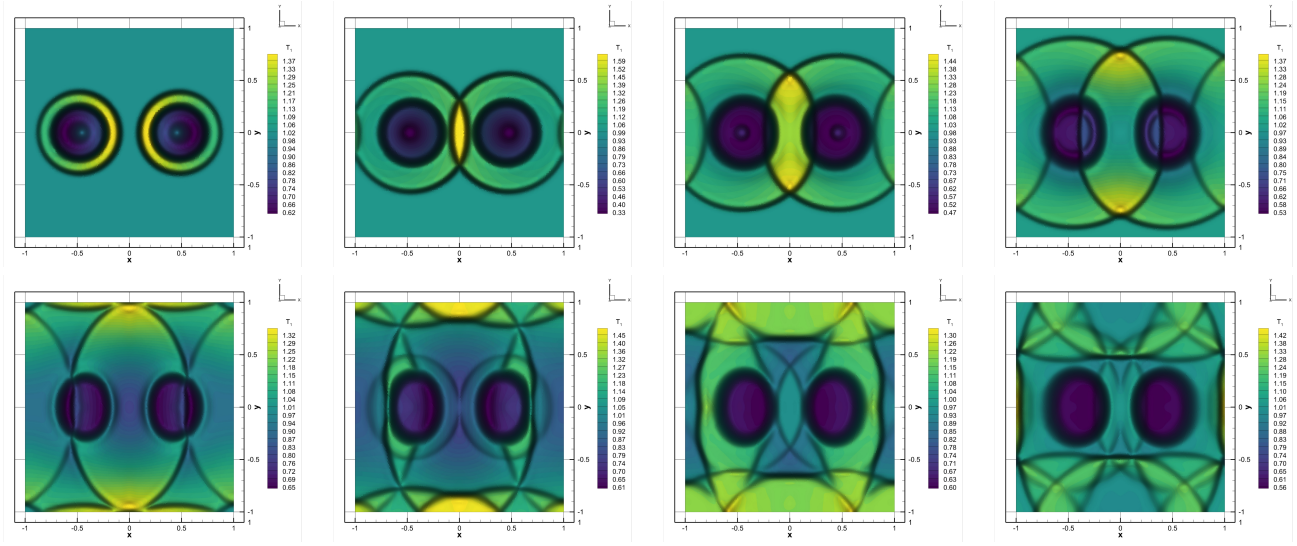

Figure 10: Interaction of two bubbles with $[\varepsilon, \alpha] = [10^{-4}, 0.8]$. Distribution of temperature T_1 at times $t = [0.1, 0.2, 0.3, 0.4, 0.5, 0.6, 0.7, 0.8]$ (from top left to bottom right). 40 contour levels within the maximum and minimum value of T_1 at each output time are used.

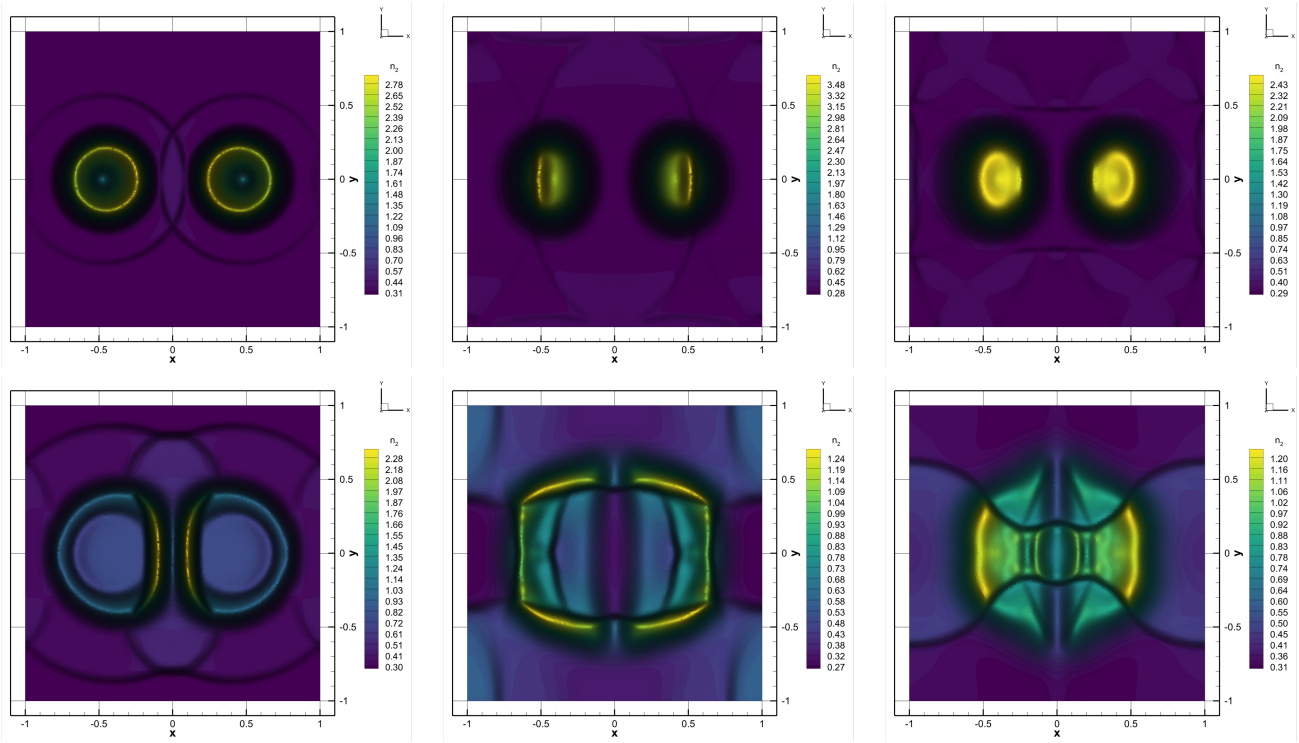

Figure 11: Interaction of two bubbles with $[\varepsilon, \alpha] = [10^{-4}, 0.8]$ (top row) and $[\varepsilon, \alpha] = [10^{-4}, 10^{-3}]$ (bottom row). Distribution of number density n_2 at times $t = 0.2$ (left), $t = 0.5$ (middle) and $t = 0.8$ (right). 40 contour levels within the maximum and minimum value of n_2 at each output time are used.

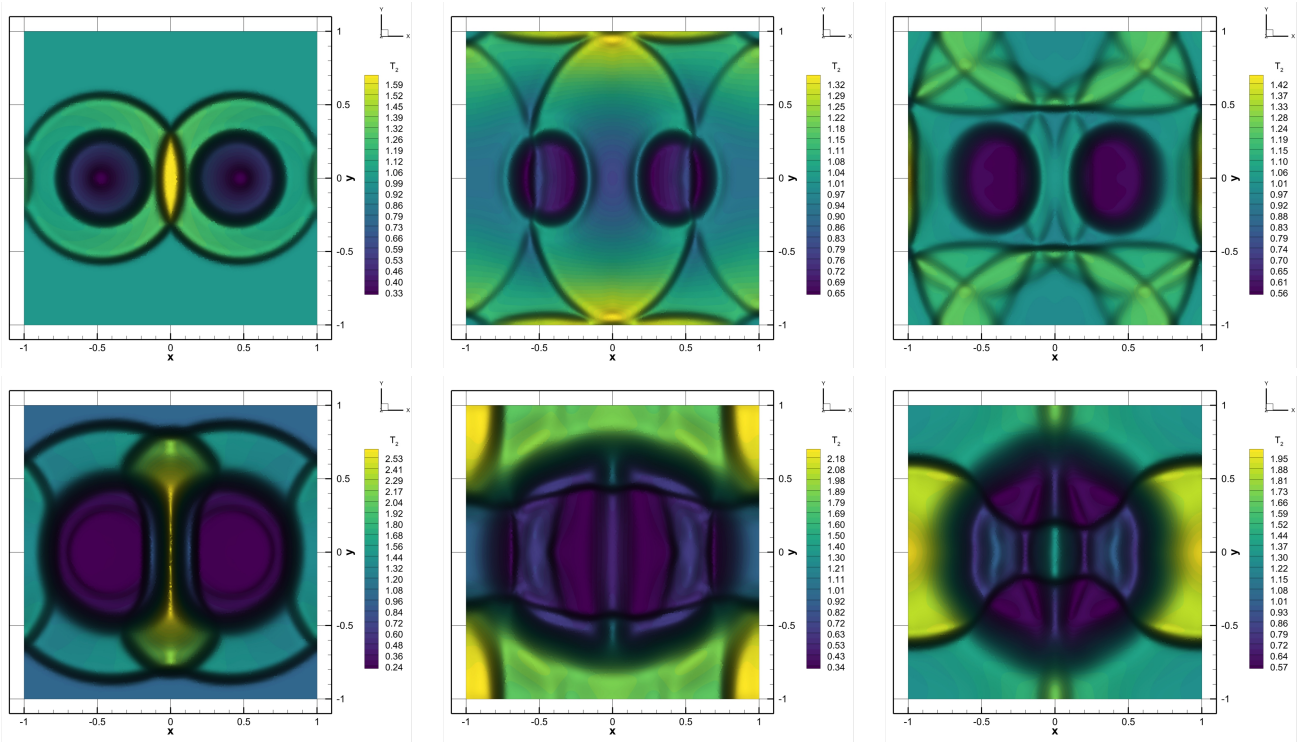

Figure 12: Interaction of two bubbles with $[\varepsilon, \alpha] = [10^{-4}, 0.8]$ (top row) and $[\varepsilon, \alpha] = [10^{-4}, 10^{-3}]$ (bottom row). Distribution of temperature T_2 at times $t = 0.2$ (left), $t = 0.5$ (middle) and $t = 0.8$ (right). 40 contour levels within the maximum and minimum value of T_2 at each output time are used.

interactions. The novel model is referred to as mixed Boltzmann–BGK model and it has proven to satisfy conservation properties and positivity for the thermodynamic quantities. The uniqueness and stability of the steady state configuration of the model has been assessed by fulfilling the so-called H-theorem, and the hydrodynamic limits of the model under different collisional regimes have been investigated. In the case of all dominant collisions, the classical Euler equations of compressible gas dynamics are retrieved at the macroscopic level, whereas in the resonant collision limit we obtain a set of Euler equations which exhibit evolution equations for densities, mean velocities and temperatures of single species.

The governing kinetic equations have then be written in dimensionless form and discretized using a global second order in velocity, space and time finite volume method while the Boltzmann collision operator is solved at the aid of a fast spectral method. A discrete velocity model on Cartesian meshes is used in the phase space while the physical space is paved with arbitrarily unstructured two-dimensional control volumes, where a Central WENO polynomial reconstruction allows high order spatial accuracy to be reached. In order to obtain a stability condition of the time step which is independent of the stiffness of the equations, Implicit-Explicit (IMEX) Runge-Kutta time stepping techniques have been employed up to second order of accuracy in time. In the case of diagonally implicit and stiffly accurate IMEX methods asymptotic preservation and accuracy have been proved for the full discrete scheme under the hypothesis of well-prepared initial data. Finally, the robustness of the proposed numerical scheme is validated against a set of test cases which involve shock waves in multiple space dimensions under different stiff regimes, and the accuracy is experimentally shown to achieve second order in space and time on smooth solutions. The code has been implemented under MPI parallelization and all test cases have been run on 64 cores to demonstrate the applicability of our algorithm to large scale HPC architectures, taking into account up to $\approx 70 \cdot 10^6$ degrees of freedom.

We plan to extend the present approach to higher order space-time schemes following the seminal works devised in [19, 20], which also include a discontinuous Galerkin (DG) space discretization along with a Linear Multistep (LM) time integrator. The possible extension of the mixed Boltzmann-BGK kinetic model to a general N-component (inert or reactive) gas mixture will be also investigated in future. Finally, we plan also to extend the present approach to ideal magnetohydrodynamics (MHD) flows to be modeled in the stiff limit by the mixture kinetic equations.

Acknowledgments

This work has been realized with the support of the Italian Ministry of Instruction, University and Research (MIUR) in the framework of the PRIN Projects 2017 No. 2017KKJP4X entitled *Innovative numerical methods for evolutionary partial differential equations and applications* and No. 2017YBKNCE entitled *Multiscale phenomena in Continuum Mechanics: singular limits, off-equilibrium and transitions*. We also acknowledge the support of the Universities of Ferrara and Parma (Italy) and of the groups GNCS and GNFM of INdAM (*Istituto Nazionale di Alta Matematica*).

References

[1] L. Boudin A. Bondesan and B. Grec. A numerical scheme for a kinetic model for mixture in the diffusive limit using the moment method. *Numer. Meth. Part. Differ. Equat.*, 35:1184–1205, 2019.

[2] P. Andries, K. Aoki, and B. Perthame. A consistent BGK–type model for gas mixtures. *J. Stat. Phys.*, 106(5):993–1018, 2002.

[3] U. M. Ascher, S. J. Ruuth, and R. J. Spiteri. Implicit-explicit Runge-Kutta methods for time-dependent partial differential equations. *Appl. Numer. Math.*, 25(2-3):151–167, 1997. Special issue on time integration (Amsterdam, 1996).

[4] Uri M. Ascher, Steven J. Ruuth, and Brian T. R. Wetton. Implicit-explicit methods for time-dependent partial differential equations. *SIAM J. Numer. Anal.*, 32(3):797–823, 1995.

[5] R. Bailo and T. Rey. Projective and Telescopic Projective Integration for Non-Linear Kinetic Mixtures. 2021.

[6] C. Baranger, Y. Dauvois, G. Marois, J. Mathé, J. Mathiaud, and L. Mieussens. A bgk model for high temperature rarefied gas flows. *European Journal of Mechanics - B/Fluids*, 80:1–12, 2020.

[7] T.J. Barth and P.O. Frederickson. Higher order solution of the Euler equations on unstructured grids using quadratic reconstruction. *AIAA paper no. 90-0013*, 28th Aerospace Sciences Meeting January 1990.

[8] P.L. Bhatnagar, E.P. Gross, and K. Krook. A model for collision processes in gases. *Phys. Rev.*, 94(3):511–524, 1954.

[9] M. Bisi, M. Groppi, and G.Spiga. Kinetic Bhatnagar-Gross-Krook model for fast reactive mixtures and its hydrodynamic limit. *Phys. Rev. E*, 81(3):036327, 2010.

[10] M. Bisi, M. Groppi, and G. Martalò. Macroscopic equations for inert gas mixtures in different hydrodynamic regimes. *J. Phys. A: Math. Theor.*, 54(8):085201, 2021.

[11] M. Bisi and S. Lorenzani. High-frequency sound wave propagation in binary gas mixtures flowing through microchannels. *Phys. Fluids*, 28(5):052003, 2016.
[12] M. Bisi, G. Martalò, and G. Spiga. Multitemperature Euler hydrodynamics for a reacting gas from a kinetic approach to rarefied mixtures with resonant collisions. *Europhys. Lett.*, 95(5):55002, 2011.
[13] M. Bisi, R. Monaco, and A.J. Soares. A BGK model for reactive mixtures of polyatomic gases with continuous internal energy. *J. Phys. A - Math. Theor.*, 51(12):125501, 2018.
[14] M. Bisi and R. Travaglini. A BGK model for mixtures of monoatomic and polyatomic gases with discrete internal energy. *Physica A: Stat. Mech. Appl.*, 547:124441, 2020.
[15] A.V. Bobylev, M. Bisi, M. Groppi, G. Spiga, and I.F. Potapenko. A general consistent BGK model for gas mixtures. *Kinet. Relat. Models*, 11(6):1377–1393, 2018.
[16] A.V. Bobylev, A. Palczewski, and J. Schneider. On approximation of the Boltzmann equation by discrete velocity models. *C. R. Acad. Sci. Paris Sér. I Math.*, 320(5):639–644, 1995.
[17] S. Boscarino, S.Y. Cho, M. Groppi, and G. Russo. BGK models for inert mixtures: comparison and applications. *Kinet. Relat. Models*, 14(5):895–928, 2021.
[18] S. Boscarino, G. Russo, and M. Semplice. High order finite volume schemes for balance laws with stiff relaxation. *Comput. & Fluids*, 169:155–168, 2018.
[19] W. Boscheri and G. Dimarco. High order finite volume schemes with IMEX time stepping for the Boltzmann model on unstructured meshes. *Comput. Methods Appl. Mech. Engrg.*, 387:114180, 2021.
[20] W. Boscheri and G. Dimarco. High order modal Discontinuous Galerkin Implicit-Explicit Runge Kutta and Linear Multistep schemes for the Boltzmann model on general polygonal meshes. *Computers and Fluids*, 233:105224, 2022.
[21] Walter Boscheri and Giacomo Dimarco. High order central weno-implicit-explicit runge kutta schemes for the bgk model on general polygonal meshes. *Journal of Computational Physics*, 422:109766, 08 2020.
[22] C. Cercignani. *The Boltzmann equation and its applications*, volume 67 of *Applied Mathematical Sciences*. Springer-Verlag, New York, 1988.
[23] S. Chapman and T. G. Cowling. *The Mathematical Theory of Non–Uniform Gases*. Cambridge University Press, 3rd edition, 1970.
[24] L. Chen and L. Schafer. Godunov-type upwind flux schemes of the two-dimensional finite volume discrete boltzmann method. *Computers and Mathematics with Applications*, 75:3105–3126, 2018.
[25] N. Crouseilles, G. Dimarco, and M. Lemou. Asymptotic preserving and time diminishing schemes for rarefied gas dynamic. *Kinet. Relat. Models*, 10(3):643–668, 2017.
[26] P. Degond. Asymptotic-preserving schemes for fluid models of plasmas. *Panoramas et Syntheses*, SMF, 2014.
[27] P. Degond and F. Deluzet. Asymptotic-preserving methods and multiscale models for plasma physics. *J. Comput. Phys.*, 336:429–457, 2017.
[28] G. Dimarco and L. Pareschi. High order asymptotic-preserving schemes for the Boltzmann equation. *C. R. Math. Acad. Sci. Paris*, 350(9-10):481–486, 2012.
[29] G. Dimarco and L. Pareschi. Asymptotic preserving implicit-explicit Runge-Kutta methods for nonlinear kinetic equations. *SIAM J. Numer. Anal.*, 51(2):1064–1087, 2013.
[30] G. Dimarco and L. Pareschi. Numerical methods for kinetic equations. *Acta Numer.*, 23:369–520, 2014.
[31] G. Dimarco and L. Pareschi. Implicit-explicit linear multistep methods for stiff kinetic equations. *SIAM J. Numer. Anal.*, 55(2):664–690, 2017.
[32] M. Dumbser and W. Boscheri. High-order unstructured Lagrangian one–step WENO finite volume schemes for non–conservative hyperbolic systems: Applications to compressible multi–phase flows. *Computers and Fluids*, 86:405–432, 2013.
[33] A. Ern and V. Giovangigli. Kinetic theory of reactive gas mixtures with application to combustion. *Transport Theory and Statistical Physics*, 32(5-7):657–677, 2003.
[34] Ben Evans, Ken Morgan, and Oubay Hassan. A discontinuous finite element solution of the boltzmann kinetic equation in collisionless and bgk forms for macroscopic gas flows. *Applied Mathematical Modelling*, 35(3):996–1015, 2011.
[35] J. H. Ferziger and H. G. Kaper. Mathematical theory of transport processes in gases. *American Journal of Physics*, 41(4):601–603, 1973.
[36] F. Filbet and S. Jin. A class of asymptotic-preserving schemes for kinetic equations and related problems with stiff sources. *J. Comput. Phys.*, 229(20):7625–7648, 2010.
[37] F. Filbet, C. Mouhot, and L. Pareschi. Solving the Boltzmann equation in N log2 N. *SIAM J. Sci. Comput.*, 28(3):1029–1053, 2007.
[38] Elena Gaburro, Walter Boscheri, Simone Chiocchetti, Christian Klingenberg, Volker Springel, and Michael Dumbser. High order direct arbitrary-lagrangian-eulerian schemes on moving voronoi meshes with topology changes. *Journal of Computational Physics*, 407:109167, 2020.
[39] V.S. Galkin and N.K. Makashev. Kinetic derivation of the gas-dynamic equation for multicomponent mixtures of light and heavy particles. *Fluid Dynam.*, 29(1):140–155, 1994.
[40] I. M. Gamba and S. H. Tharkabhushanam. Spectral-Lagrangian methods for collisional models of non-equilibrium statistical states. *J. Comput. Phys.*, 228(6):2012–2036, April 2009.
[41] M. Groppi and G. Spiga. A Bhatnagar–Gross–Krook-type approach for chemically reacting gas mixtures. *Phys. Fluids*, 16(12):4273–4284, 2004.
[42] M. Groppi, G. Spiga, and F. Zus. Euler closure of the Boltzmann equations for resonant bimolecular reactions. *Phys. Fluids*, 18(5):057105, 2006.
[43] J.R. Haack, C.D Hauck, and M.S. Murillo. A conservative, entropic multispecies BGK model. *J. Stat. Phys.*, 168(4):826–856, 2017.
[44] C. Hu and C.W. Shu. Weighted essentially non-oscillatory schemes on triangular meshes. *Journal of Computational Physics*, 150:97–127, 1999.
[45] Shashank Jaiswal, Alina A. Alexeenko, and Jingwei Hu. A discontinuous Galerkin fast spectral method for the full Boltzmann equation with general collision kernels. *J. Comput. Phys.*, 378:178–208, 2019.
[46] S. Jin. Asymptotic preserving (AP) schemes for multiscale kinetic and hyperbolic equations: a review. *Riv. Math. Univ. Parma (N.S.)*,

3(2):177–216, 2012.
[47] C. Klingenberg, M.Pirner, and G. Puppo. A consistent kinetic model for a two-component mixture with an application to plasma. *Kinet. Relat. Models*, 10(2):445–465, 2017.
[48] J.M. Reese L. Wu, J. Zhang and Y. Zhang. A fast spectral method for the Boltzmann equation for monoatomic gas mixtures. *Journal of Computational Physics*, 298:602–621, 2015.
[49] Q. Li and L. Pareschi. Exponential Runge-Kutta for the inhomogeneous Boltzmann equations with high order of accuracy. *J. Comput. Phys.*, 259:402–420, 2014.
[50] F.J. McCormack. Construction of linearized kinetic models for gaseous mixtures and molecular gases. *Phys. Fluids*, 16(12):2095–2105, 1973.
[51] L. Mieussens. Discrete velocity model and implicit scheme for the BGK equation of rarefied gas dynamics. *Mathematical Models and Methods in Applied Sciences*, 10(08):1121–1149, 2000.
[52] L. Pareschi and G. Russo. Numerical solution of the Boltzmann equation I: Spectrally accurate approximation of the collision operator. *SIAM journal on numerical analysis*, 37:1217–1245, 2000.
[53] Sandra Pieraccini and Gabriella Puppo. Implicit-explicit schemes for BGK kinetic equations. *J. Sci. Comput.*, 32(1):1–28, 2007.
[54] M. Pirner. *Kinetic modelling of gas mixtures*. Würzburg University Press, 2018.
[55] A.H. Stroud. *Approximate Calculation of Multiple Integrals*. Prentice-Hall Inc., Englewood Cliffs, New Jersey, 1971.
[56] Wei Su, Peng Wang, Yonghao Zhang, and Lei Wu. Implicit discontinuous Galerkin method for the Boltzmann equation. *J. Sci. Comput.*, 82(2):Art. 39, 35, 2020.
[57] B.N. Todorova and R. Steijl. Comparison of Discrete Velocity Method and Gas-Kinetic Method for Binary Gas Mixtures. *Journal of Thermophysics and Heat Transfer*, 34:45–56, 2020.
[58] R. Wang Y. Zhang, L. Zhu and Z. Guo. Discrete unified gas kinetic scheme for all knudsen number flows. iii. binary gas mixtures of maxwell molecules. *Phys. Rev. E*, 97:053306, 2018.